

Lappeenranta University of Technology
LUT School of Technology
Master's Degree Programme in Energy Technology

Elina Hujala

EVALUATION OF BUBBLE FORMATION AND BREAK UP IN SUPPRESSION POOLS BY USING PATTERN RECOGNITION METHODS

Supervisor: D.Sc. Vesa Tanskanen
Examiners: Professor Riitta Kyrki-Rajamäki
D.Sc. Vesa Tanskanen

ABSTRACT

Lappeenranta University of Technology
LUT School of Technology
Master's Degree Programme in Energy Technology

Elina Hujala

Evaluation of Bubble Formation and Break Up in Suppression Pools by Using Pattern Recognition Methods

Master's Thesis
2013

65 pages, 35 figures, 4 tables and 6 appendices.

Examiners: Professor Riitta Kyrki-Rajamäki
D.Sc. Vesa Tanskanen

Keywords: suppression pool, bubble break up, BWR, pattern recognition

During a possible loss of coolant accident in BWRs, a large amount of steam will be released from the reactor pressure vessel to the suppression pool. Steam will be condensed into the suppression pool causing dynamic and structural loads to the pool.

The formation and break up of bubbles can be measured by visual observation using a suitable pattern recognition algorithm. The aim of this study was to improve the preliminary pattern recognition algorithm, developed by Vesa Tanskanen in his doctoral dissertation, by using MATLAB. Video material from the PPOOLEX test facility, recorded during thermal stratification and mixing experiments, was used as a reference in the development of the algorithm.

The developed algorithm consists of two parts: the pattern recognition of the bubbles and the analysis of recognized bubble images. The bubble recognition works well, but some errors will appear due to the complex structure of the pool. The results of the image analysis were reasonable. The volume and the surface area of the bubbles were not evaluated. Chugging frequencies calculated by using FFT fitted well into the results of oscillation frequencies measured in the experiments.

The pattern recognition algorithm works in the conditions it is designed for. If the measurement configuration will be changed, some modifications have to be done. Numerous improvements are proposed for the future 3D equipment.

TIIVISTELMÄ

Lappeenrannan teknillinen yliopisto

Teknillinen tiedekunta

Energiateknikan koulutusohjelma

Elina Hujala

Kuplan muodostumisen ja luhistumisen arviointi lauhdutusaltaissa hahmontunnistuksen avulla

Diplomityö

2013

65 sivua, 35 kuvaaa, 4 taulukkoa ja 6 liitettä.

Tarkastajat: Professori Riitta Kyrki-Rajamäki
TkT Vesa Tanskanen

Hakusanat: lauhdutusallas, kuplan luhistuminen, BWR, hahmontunnistus

Keywords: suppression pool, bubble break up, BWR, pattern recognition

Mahdollisen jäähytteenmenetysonnettomuuden aikana suuri määrä höyryä vapautuu reaktorin paineastiasta lauhdutusaltaaseen. Höyry tiivistyy lauhdutusaltaassa aiheuttaen dynaamisia ja rakenteellisia kuormituksia altaaseen.

Kuplien muodostumista ja luhistumista voidaan mitata visuaalisin havainnoin sopivan hahmontunnistusalgoritmin avulla. Tämän työn tarkoituksena oli parantaa Vesa Tanskasen väitöskirjassaan kehittämää hahmontunnistusalgoritmia MATLAB:lla. PPOOLEX-laitteistolla mitattua lämmön kerrostumis- ja sekoittumiskokeissa kuvattuja videoita käytettiin referenssinä algoritmia kehitettäessä.

Algoritmi koostuu kahdesta osasta: kuplien hahmontunnistuksesta sekä tunnistettujen kuplakuvien analysoinnista. Kuplien tunnistus toimii hyvin, mutta laitteiston monimutkaisesta rakenteesta johtuen joitakin virheitä esiintyy. Kuvien analysoinnin tulokset ovat järkeviä. Kuplien tilavuutta tai pinta-alaa ei määritetty. Chugging-taajuudet, jotka laskettiin käyttäen FFT:tä, sopivat hyvin kokeissa mitattuihin oskilloointitaajuksiin.

Algoritmi toimii olosuhteissa, joihin se on suunniteltu. Jos mittauslaitteistossa muutetaan joitain, muutoksia täytyy tehdä myös algoritmiin. Työssä ehdotetaan myös lukuisia parannuksia tulevaan 3D-laitteistoon.

Acknowledgements

I would like to thank my supervisor D.Sc. Vesa Tanskanen (and his old Nissan) for inspiration and support during this work. My warmest thanks to professor Riitta Kyrki-Rajamäki, who let me be free and do what I wanted. All other co-workers at the laboratory of nuclear engineering and nuclear safety research unit I would like to thank for the cosy atmosphere during working hours.

I thank the department of mathematics and physics old coffee group (especially Riitta, Miika, Erik, Matti A., Virpi, Juha, Jari and Kirsi) and the children's room boys for the good old days and games.

Last but not least thanks to Aki who taught me how to chop and change with and without MATLAB.

Lappeenranta, 21st March, 2013

Elina Hujala

Contents

1	Introduction	9
1.1	Aim of the Study	11
1.2	Outline of the Thesis	12
2	PPOOLEX Test Facility	13
2.1	PPOOLEX Test Vessel	13
2.2	Measurement Instrumentation	14
2.3	Data Acquisition	15
2.4	CCTV System and Video Cameras	16
3	The Thermal Stratification and Mixing Experiments MIX-01, MIX-02, and MIX-03	18
3.1	The Initial State Arrangements of the Experiments	18
3.2	Thermal Stratification Period	19
3.3	Mixing Period and Steam/Water Interface Oscillations in the Blow-down Pipe	20
4	Introduction to Image Processing and Pattern Recognition Using MATLAB	23
4.1	Digital Image Representation	23
4.2	Basic Operation with Image Processing Toolbox	24
4.2.1	Image Reconstruction	25
4.2.2	Pattern Recognition and Image Analysis	25
5	Pattern Recognition Algorithm	28
5.1	From Recorded Video to Image Sequence	28
5.2	Structure of the Pattern Recognition Algorithm	29
5.2.1	Init_Ref_Image_(Steam/Air/Jet) functions	31
5.2.2	Pattern Recognition Loop	34
6	Image Analysis	35
7	Results and Discussion	40

7.1	Results of the Pattern Recognition	40
7.2	Results of the Image Analysis	42
7.3	Calculation of the Chugging Frequency	43
7.4	Feasibility of the Pattern Recognition Algorithm	46
8	Conclusions	47
8.1	Recommendations for the Future 3D Set-Up	49
	Bibliography	50
	Appendix I Test Vessel Measurements	
	Appendix II Temperature Measurements	
	Appendix III Flow Diagram	
	Appendix IV 1 second of Air Bubbles	
	Appendix V 1 second of Steam Bubbles	
	Appendix VI 1 second of Jets	

List of symbols and abbreviations

Symbols

Symbol	Description	Unit
α	angle	rad
d	distance between camera and window, diameter of pipe	m
D	distance between object (pipe) and window	m
f	frequency	Hz
$f(x, y)$	function $f(x, y)$	-
h	height of pipe	m
$h(O)$	height of object	m
$h(a)$	height of image in air	m
$h(w)$	height of image in water	m
h'	observed height of pipe	m
i	incident angle of refraction	rad
I	image matrix, distance between image and the camera	-, m
J	function	-
L	arbitrary label matrix	-
M	number of matrix rows	-
N	number of matrix columns	-
O	distance between object and camera	m
r	angle of refraction	rad
R	reflecting surface radius of camera	m
(x, y)	location of a pixel whose brightness is given by the function $f(x, y)$	-
X, Y, Z	arrays	-

Abbreviations

AVI	audio video interleave
BWR	boiling water reactor
CCTV	closed circuit television
CFD	computational fluid dynamics
CONDEX	condensation experiments project with PPOOLEX facility
ECCS	emergency core cooling system
EMS	effective momentum source
EXCOP	experimental studies on containment phenomena project
FFT	fast Fourier transform
FINNUS	the Finnish Research Programme on Nuclear Power Plant Safety
fps	frames per second
JPG	Joint Photographic Group
LOCA	loss of coolant accident
LUT	Lappeenranta University of Technology
MIX	mixing experiment series
MSLB	main steam line break
PACTEL	parallel channel test loop
POOLEX	condensation pool experiments project
PPOOLEX	pressurized condensation pool facility
RGB	red-green-blue (truecolor) image
ROI	region of interest
SAFIR	Safety of Nuclear Power Plants - Finnish National Research Programme
STR	stratification and mixing experiments
TVO	Teollisuuden Voima Oyj
VTT	Technical Research Centre of Finland

1 Introduction

All boiling water reactors (BWR) in the Nordic countries, including Olkiluoto 1 and 2, are of Asea-Atom design, [1]. In this design the pressure suppression system is similar to MARK II, the pressure suppression system design of General-Electric, with vertical blowdown pipes as shown in Figure 1.1. The suppression pool serves as the major heat sink for the condensation of steam.

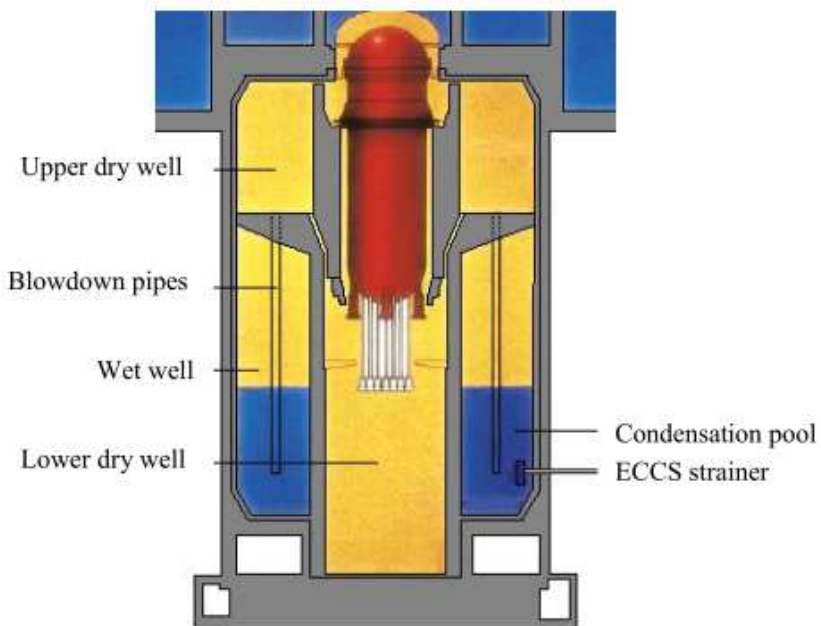


Figure 1.1. Schematic of the Finnish type BWR containment.

During a possible loss of coolant accident (LOCA), such as a main steam line break (MSLB) in Finnish type boiling water reactors, a large amount of condensable gas will be released from the reactor pressure vessel. The dry well will be rapidly pressurized. The steam will be blown from the upper dry well of the containment to the suppression pool through blowdown pipes.

At the beginning, the blowing gas consists only of non-condensable nitrogen, but later on it will be mixed with condensable steam. Steam will be condensed on the

dry well walls, inside the blowdown pipe, and into the suppression pool water, but non-condensable gases will eventually accumulate to the wet well gas space, [2]. Rapid condensation of the steam causes both dynamic and structural loads to the suppression pool. There might also be a risk that the gas discharging to the pool could push its way to the emergency core cooling systems (ECCS) and undermine their performance, [3, 4].

Nuclear Safety Research Unit at Lappeenranta University of Technology (LUT) has done nuclear safety research for over thirty years. The Finnish type BWR condensation pool studies started in 2001 within the Finnish Research Programme on Nuclear Power Plant Safety (FINNUS). The test programme was partially funded by Teollisuuden Voima Oyj (TVO), [4]. Experimental studies continued in 2003 in the Safety of Nuclear Power Plant - Finnish National Research Program (SAFIR) project Condensation Pool Experiments (POOLEX) whose main objective was to increase the understanding of different phenomena in the condensation pool during steam injection.

In these research projects, the formation, size, and distribution of non-condensable gas and steam bubbles in the condensation pool were studied with an open scaled down pool test facility. Also the effect of non-condensable gas on the performance of an emergency core cooling system pump was examined. The experiments were modeled with computational fluid dynamics (CFD) and structural analysis codes at VTT [4, 5]. The CFD calculations of the same experiments started at LUT in 2005 [6].

In 2006, a new test facility for BWR containment studies was designed and constructed at the Nuclear Safety Research Unit, [2, 7]. The facility called PPOOLEX modelled both dry and wet well condensation pool compartments of the containment. SAFIR project Condensation Experiments with the PPOOLEX Facility (CONDEX) started in 2007, [8]. During the years 2007–2010, various experiments were carried out with the PPOOLEX facility. Experiments began by running characterizing tests [8] followed by steam line rupture experiments and the first series of thermal stratification and mixing experiments (STR-01, . . . , STR-06) [9]. Also the test series focusing on steam condensation on dry well compartment, experiments to study the effect of the Forsmark type blowdown pipe outlet collar design on loads caused by the chugging phenomenon, eleven experiments studying the effect of the number of blowdown pipes on loads caused by chugging phenomenon, and experiments focusing on dynamic loading during steam discharge were carried out [10].

The current SAFIR project with the PPOOLEX test facility, EXCOP (EXperimental studies on COntainment phenomena Project), was started in 2011 [11]. The main objective of the project was to improve the understanding and increase the fidelity in the quantification of different phenomena inside the dry well and wet well compartments of BWR containment during steam discharge [11]. EXCOP is going on as a part of the SAFIR2014 project.

The results of the experiments have been used for several different purposes including comparing condensation rates between the experiments and CFD simulations. The CFD simulations were made in the EU projects NURESIM, NURISP, and NURENEXT [12]. The NURENEXT project is currently going on. Measured data (pressure, temperature etc.) gives valuable knowledge of the validity of computer simulations, whereas the validation of bubble formation, break up, size distribution, and form is not straightforward without visual observation. The bubble break up and size distribution have been modeled in various research areas e.g. in chemical engineering [13–15]. At the same time, the popularity of the pattern recognition is increasing in the two phase flow analysis [16, 17]. For visual observation the POOLEX and PPOOLEX test facilities have used several digital normal and high speed cameras. A preliminary pattern recognition procedure for the visualization of the bubbles was made by Vesa Tanskanen during the CONDEX and NURISP projects [12].

1.1 Aim of the Study

The main objective of this thesis is to improve the pattern recognition procedure [12] and image analysis of bubble formation and break up. The improvements consist of better removal of image background, more exact bubble boundary recognition, and more automated procedure. In the old pattern recognition procedure, possible errors were removed manually without automated recognition.

As the test vessel contains various instrumentations, the blowdown pipe is purposely non-axisymmetrical and the lighting of the closed pool is difficult to carry out, the idea was to clarify how much of the inhomogeneity of the pool lighting and structure is possible to be reasonably removed only by image reconstruction and pattern recognition. The preliminary pattern recognition algorithm was made by using a single camera. The view has now been broadened into a dual camera case.

In the fall 2013, Nuclear Safety Research Unit will have three high speed digital cameras for 3D imaging. With these cameras it will be possible to find out the volumetric sizes and forms of the bubbles. With the 2D pattern recognition algorithm and image analysis procedure it will be simpler to find out image reconstruction solutions and ideas for the future 3D studies.

1.2 Outline of the Thesis

In this chapter, the background and main objective of the study are presented. In chapter 2, the PPOOLEX test facility, including instrumentation, and digital cameras used in the experiments, will be introduced. Chapter 3 will introduce three blowdown experiments; MIX-1, MIX-2, and MIX-3; on which the pattern recognition algorithm is based. Chapter 4 contains a short introduction to image processing, pattern recognition, and image analysis by using MATLAB. In chapter 5, the improved pattern recognition algorithm will be described in detail. Chapter 6 will analyse bubble images of the pattern recognition algorithm. Chapter 7 will introduce the results of the pattern recognition algorithm and image analysis. Chapter 8 contains future recommendations, plans, and the conclusion of the thesis.

2 PPOOLEX Test Facility

At LUT, the condensation studies were started with an open pool test facility (POOLEX) modelling the suppression pool of the BWR containment. The facility was replaced with a more versatile PPOOLEX facility in the end of 2006 [11]. In this chapter, the main features of the PPOOLEX test facility are introduced.

2.1 PPOOLEX Test Vessel

The main component of the PPOOLEX test facility is the approximately 31 m^3 test vessel, with the height of 7.45 m and diameter of 2.4 m. It consists of two compartments: the upper dry well compartment and the lower wet well compartment, as shown in Figure 2.1.

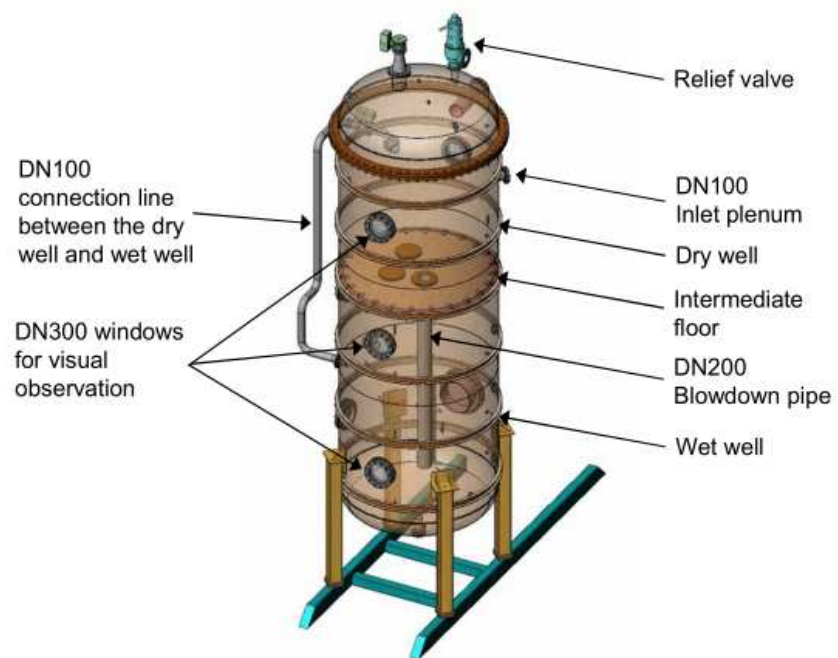


Figure 2.1. PPOOLEX test vessel.

The test vessel can be operated at temperatures up to 190 °C and at overpressures 0.4 MPa or at underpressures down to 0.05 MPa. The test vessel is assembled of three separate stainless steel plate cylinders and two dome segments. Dry well and wet well compartments are separated with an intermediate floor to scale the compartments volumetrically according to the compartment volumes of Olkiluoto 1 and 2 containment buildings (scale ratio approximately 1:320) [2, 10].

The blowdown pipe leads from the dry well to the wet well through the intermediate floor. It is possible to use different pipe lengths and diameters. In this work, DN200 (219.1 × 2.5 mm) stainless steel blowdown pipe has been used. The pipe is located inside the pool non-axisymmetrically in such a way that it is 300 mm aside from the centre of the condensation pool.

The steam used in the experiments was generated by the PACTEL test facility, which has a core section of 1 MW heating power and three horizontal steam generators. A steam line connects the PACTEL steam generator and the inlet plenum which penetrates through the thermally insulated side wall of the dry well. A relief valve connection is mounted on the top of the vessel head. The maintenance and modifications of the instrumentation can be made with a removable vessel head and through a DN500 manhole in the wet well wall. A DN100 drain valve is connected to the bottom of the pool. For the visual observation there are several windows in the walls of both compartments and at the bottom of the wet well [8].

The main parameters and dimensions of the PPOOLEX test facility are itemized in Table 2.1.

2.2 Measurement Instrumentation

The instrumentation applied in the experiments varies from test to test depending on the experiment needs. The normal instrumentation consists of several thermocouples for measuring steam, pool water, and structure temperatures and pressure transducers for observing pressure in the dry well, inside the blowdown pipe, at the bottom of the suppression pool, or in the wet well gas space (T or TC, P and C in the figures). The vortex flow meter (F) has been used to measure the steam flow rate. Also strain gauges (S) and valve position sensors are often used [18].

For the thermal stratification and mixing experiment series, a comprehensive net

Table 2.1. The main parameters and dimensions of PPOOLEX test facility [2].

Parameter	Value
Total volume	31.1 m ³
Volume of the dry well compartment	13.3 m ³
Volume of the wet well compartment	17.8 m ³
Total height	7.45 m
Height of the dry well compartment	3.18 m
Height of the wet well compartment	4.27 m
Outer diameter of the test vessel	2.4 m
Maximum overpressure	0.40 MPa
Maximum underpressure	0.05 MPa
Maximum pressure difference across the intermediate floor	0.20 MPa
Vessel head wall thickness	10 mm
Bottom end wall thickness	10 mm
Thickness of the lowest wall segment	10 mm
Thickness of the other wall segments	8 mm
Construction material	Stainless steel EN1.4301
Default blowdown pipe size	DN200
Default submerged part of blowdown pipes	~ 1 m
Default material of blowdown pipes	Stainless steel AISI304L

of thermocouples was installed into the blowdown pipe with the conventional set of instrumentation. A typical PPOOLEX test vessel measurement instrumentation is presented in Figure 2.2.

2.3 Data Acquisition

National Instruments PXIE PC-driven measuring software with LabVIEW 2011 was used for data acquisition. For monitoring and recording the measurements of PACTEL, an in-house software applying National Instruments FieldPoint measurement software was used. More detailed information on data acquisition and measuring software is presented by Räsänen [19].

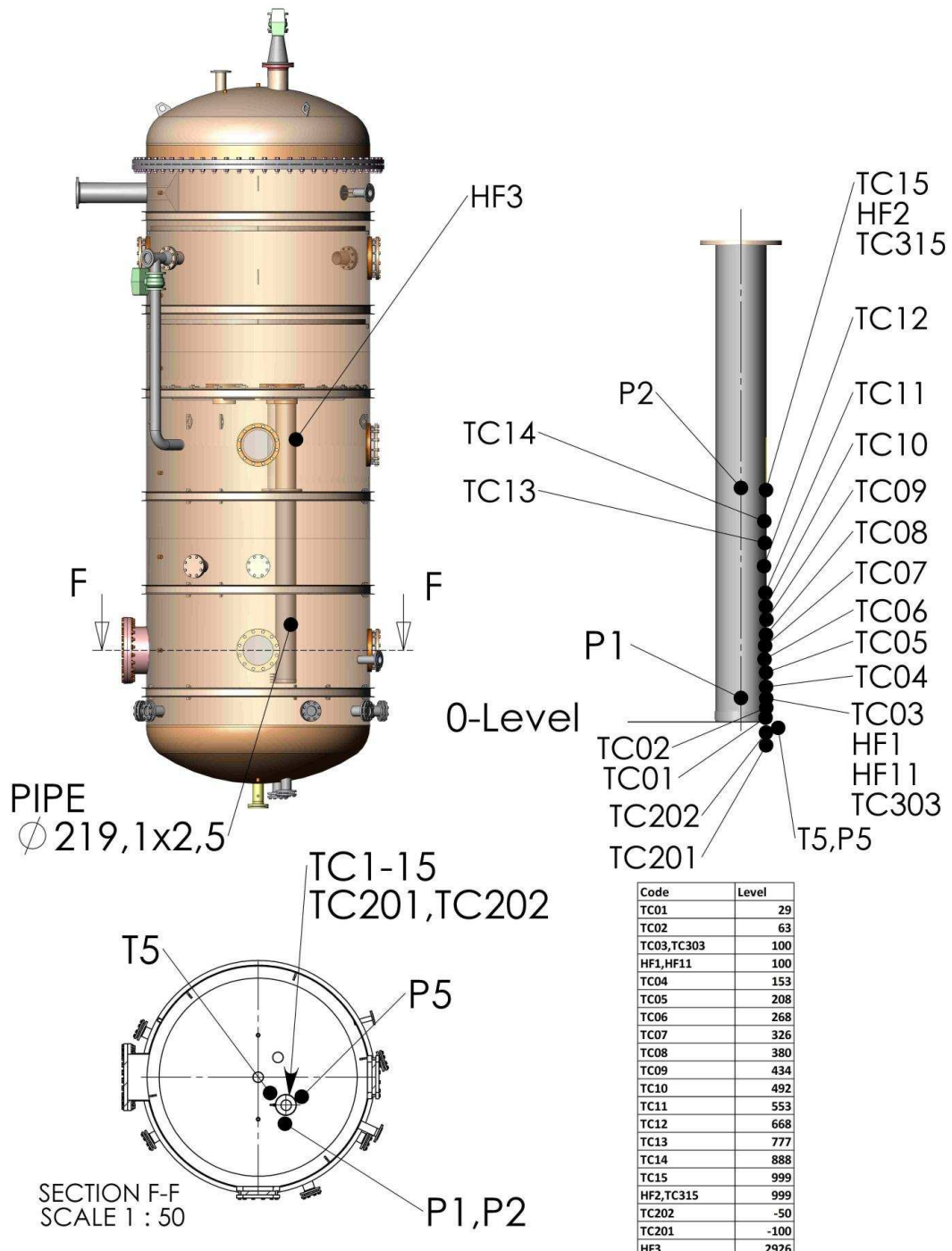


Figure 2.2. Typical measurement instrumentation of the PPOOLEX test vessel [18].

2.4 CCTV System and Video Cameras

In MIX-01, MIX-02, and MIX-03 tests, four different cameras were used; three normal (25 fps) speed cameras at the points 90°, at the bottom of the pool and on the wall of the dry well and a Phantom v.9.1 high speed camera at the point

0° , as shown in Figure 2.3. A videocassette recorder and a quad processor were used for visual observation. The digital color quad processor divides a TV screen into four parts of same size and makes it possible to look at and record the view of four cameras at the same time on the same screen.

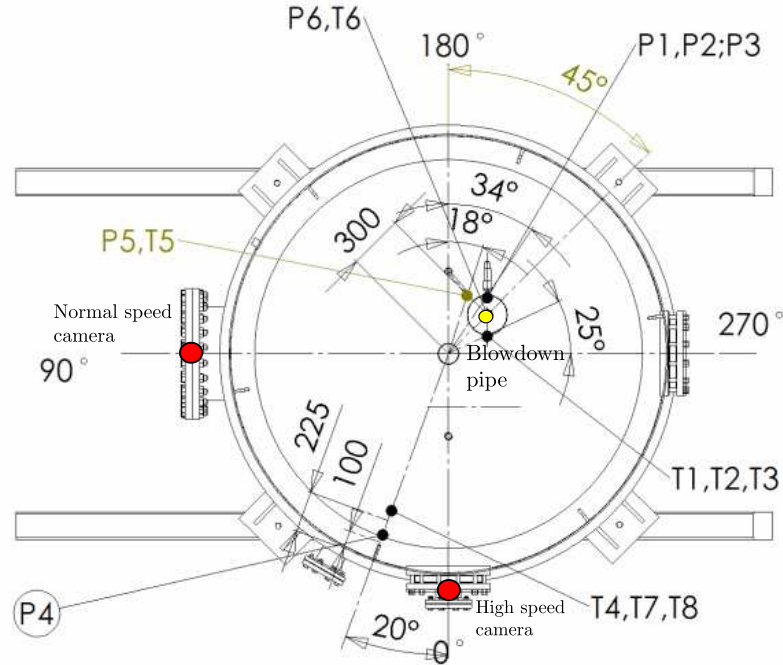


Figure 2.3. Position of the cameras. High speed camera at the point 0° (red dot), normal speed camera at the point 90° (red dot) and normal speed camera at the bottom of the pool under the blowdown pipe (yellow dot).

3 The Thermal Stratification and Mixing Experiments MIX-01, MIX-02, and MIX-03

In June–October 2012 in the EXCOP project, a series of six experiments were made. The main objective of the thermal stratification and mixing experiments, called MIX-01, . . . , MIX-06, was to generate data for the development of the Effective Momentum Source (EMS) model in the GOTHIC code [20]. A large amount of video material was recorded during the experiments. These video tapes of the experiments were remarkably useful for pattern recognition. This work focusses on the experiments MIX-01, MIX-02, and MIX-03, since the recorded video material of these three experiments was used to create an improved version of the pattern recognition algorithm.

3.1 The Initial State Arrangements of the Experiments

Before the tests, the wet well pool was filled with isothermal water to the level of 2.09 m to drown the outlet of the blowdown pipe one metre underwater. Hence, the wet well gas space was approximately 2.2 m in height. Initially, the dry well compartment was filled with air at atmospheric pressure. The initial conditions of the experiments are listed in Table 3.1.

After steam started to flow, the dry well compartment was filled with steam that mixed with the initial air content. The increased pressure in the dry well pushed the water level in the blowdown pipe downward in such a way that after a while the air/steam flow into the wet well pool started. Due to the temperature dif-

Table 3.1. Parameter values of the MIX-01, MIX-02, and MIX-03 experiments.

Experiment	MIX-01	MIX-02	MIX-03	Unit
Initial parameter values of the experiments				
Initial water level	2.09	2.09	2.09	m
Initial water temperature	13	13	13	°C
Steam source pressure	0.55–0.6	0.53–0.6	0.50–0.6	MPa
Steam flow rate	50–350	10–430	80–440	g s ⁻¹
Parameters of the heat-up phase of the experiments				
Time period	39–553	26–520	33–534	s
Steam flow rate	~ 210	~ 200	~ 205	g s ⁻¹
Initial dry well structural temperature	29	35	35	°C
Final dry well structural temperature (bottom/wall)	71/128	83/129	88/129	°C
Water temperature	13 → 31	13 → 15	13 → 15	°C

ference between the steam and the cool dry well compartment, the condensation of steam to dry well walls and structures may occur before steam even flows to the blowdown pipe. For this reason, the dry well structures were heated up to the level of 130 °C with a 190–240 g s⁻¹ steam mass flow rate. The parameters of the heat-up phase of the experiments are shown in Table 3.1. All experiments consisted of a period of stratification with a small steam mass flow and a mixing period of rapidly increased steam flow [18].

3.2 Thermal Stratification Period

When the air/steam discharge to the wet well was initiated, the pressure of the gas space of wet well compartment was increased. As the flow changed to pure steam flow, the pressure build-up stabilized. Due to the pressure increase, the temperature of the gas space was increased. The main source of heat is the conduction via intermediate floor and the walls of the test vessel and the convection from the uppermost layers of water to the wet well compartment. At the same time, the increased temperature of the gas space stratifies in such a way that the temperature was higher at the top of the pool than the temperature on the surface of water.

Similar thermal stratification occurred in the wet well pool water. During the heat-up period, the pool water inventory was heated up by 2 °C. As the desired dry well temperature was reached, the steam flow rate was decreased rapidly to

a level of $85\text{--}105 \text{ g s}^{-1}$. With this lower flow rate most of the steam condensed inside the blowdown pipe and water temperature under the blowdown pipe outlet remained constant. Above the pipe outlet, the water temperature was stratified similarly as in the gas space; the temperature increased towards the surface of water. The thermal stratification period was carried on until the desired temperature difference between the bottom of the pool and the surface of water was reached.

3.3 Mixing Period and Steam/Water Interface Oscillations in the Blowdown Pipe

When the desired temperature difference was reached, the steam mass flow rate was increased rapidly to a value of $300\text{--}425 \text{ g s}^{-1}$. The purpose of increasing the flow rate was to get the water inventory of the condensation pool mixed totally, and thus, the thermal stratification was broken. The total mixing of the pool water took approximately $150\text{--}300 \text{ s}$ depending on the original temperature of the water.

Different steam mass flow rates were tested in the MIX-01, MIX-02, and MIX-03 experiments. MIX-01 had the smallest steam mass flow rate of 325 g s^{-1} and the total pool mixing took the longest time: 300 s . In MIX-02, the steam mass flow rate was approximately 375 g s^{-1} with a mixing time of 250 s . With the largest steam mass flow rate 425 g s^{-1} , the mixing time was only 150 s in the experiment MIX-03. The temperature difference between the bottom and the surface of the condensation pool in the experiments is shown in Figure 3.1. In all experiments, the pool water remained isothermal as long as steam was blown into the pool.

During the increased steam mass flow rate, the surface of the water and steam in the blowdown pipe started to oscillate. The oscillation is a result of the chugging condensation mode [21]. The oscillation was observed during 10 s , starting at 30 s after the steam flow rate was increased. The amplitude of the oscillation was measured by using fifteen thermal transducers on the blowdown pipe wall. The amplitude varied between $29\text{--}999 \text{ mm}$ depending on the experiment. The frequency of the oscillations was $0.60\text{--}1.82 \text{ Hz}$ with an average of 1 Hz . [18].

Stratification, mixing and oscillation related observations, as well as observations in the wet well gas space are listed in Table 3.2. Abbreviations of the thermocouples are explained in Appendices I and II in Figures I.1 and II.1.

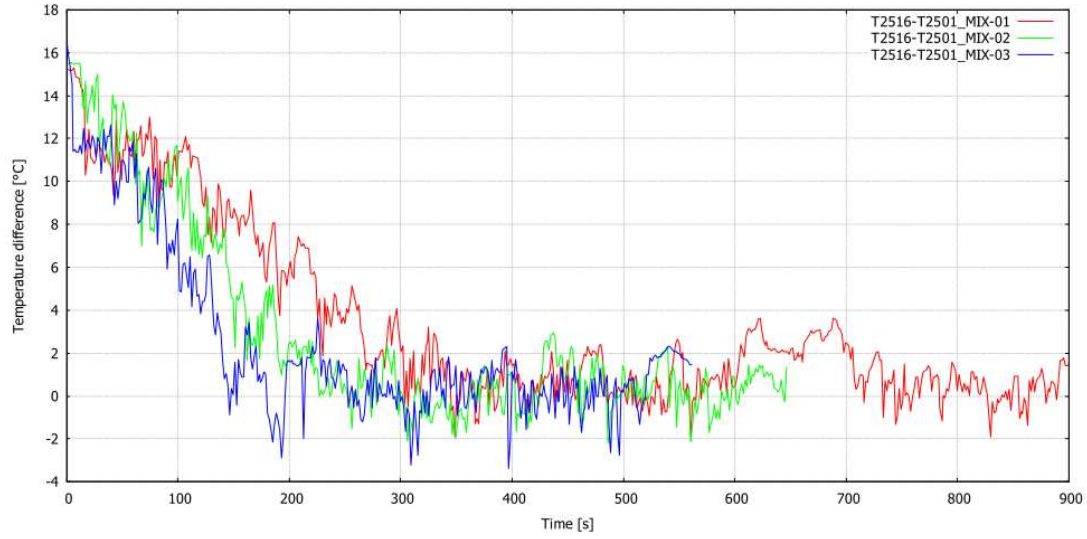


Figure 3.1. Temperature difference between the bottom and surface of the condensation pool (T2516-T2501) in MIX-01, MIX-02, and MIX-03 experiments. 0 s is the moment when the steam flow rate was increased to mix the pool water inventory [18]. Abbreviations of the thermocouples are explained in Appendix II.

Table 3.2. Stratification, mixing and oscillation related observations and observations in the wet well gas space during the experiments.

Experiment	MIX-01	MIX-02	MIX-03	Unit
Observations in the wet well gas space during the experiments				
Initial gas temperature	22–26	21–28	22–29	°C
Max. T2204 temperature	77	75	75	°C
T2204 increase	51	47	46	°C
Max. temperature difference between T2204 and T2208	25	26	25	°C
Stratification related observations of the experiments				
Time period	553–2620	520–2260	534–2290	s
Initial water temperature	15	15	15	°C
Steam flow rate	~ 90	~ 100	~ 90	g s^{-1}
Stratification time	2067	1740	1756	s
Final water temperature of T2501 and T2516	16–31	16–31	16–32	°C
Final temperature difference between T2501 and T2516	15	15	16	°C
Mixing related observations of the experiments				
Time period	2620–3500	2260–2900	2290–2800	s
Steam flow rate	~ 325	~ 375	~ 425	g s^{-1}
Mixing time	300	250	150	s
Isothermal temperature	27 → 39	26 → 35	23 → 34	°C
Oscillation related observations of the experiments				
Time period	2650.36–2659.96	2290.84–2299.90	2320.41–2329.90	s
Amplitude	29–668	268–999	100–668	mm
Average amplitude	318	533	493	mm
Frequency	0.80–1.56	0.77–1.06	0.60–1.23	Hz
Average frequency	0.99	0.90	0.90	Hz

During the thermal stratification and mixing experiments, three different shapes of bubble blowing modes were observed. Air/steam mixture and small mass

flow rate of pure steam caused irregular swarms of small bubbles into the water which rose upwards near to the blowdown pipe. With larger mass flow rates, mushroom-type bubbles were inflated which arose along the pipe as well. In chugging condensation mode, a typical bubble mode was a jet which remained under the blowdown pipe outlet. Different bubble modes are shown in Figure 3.2.

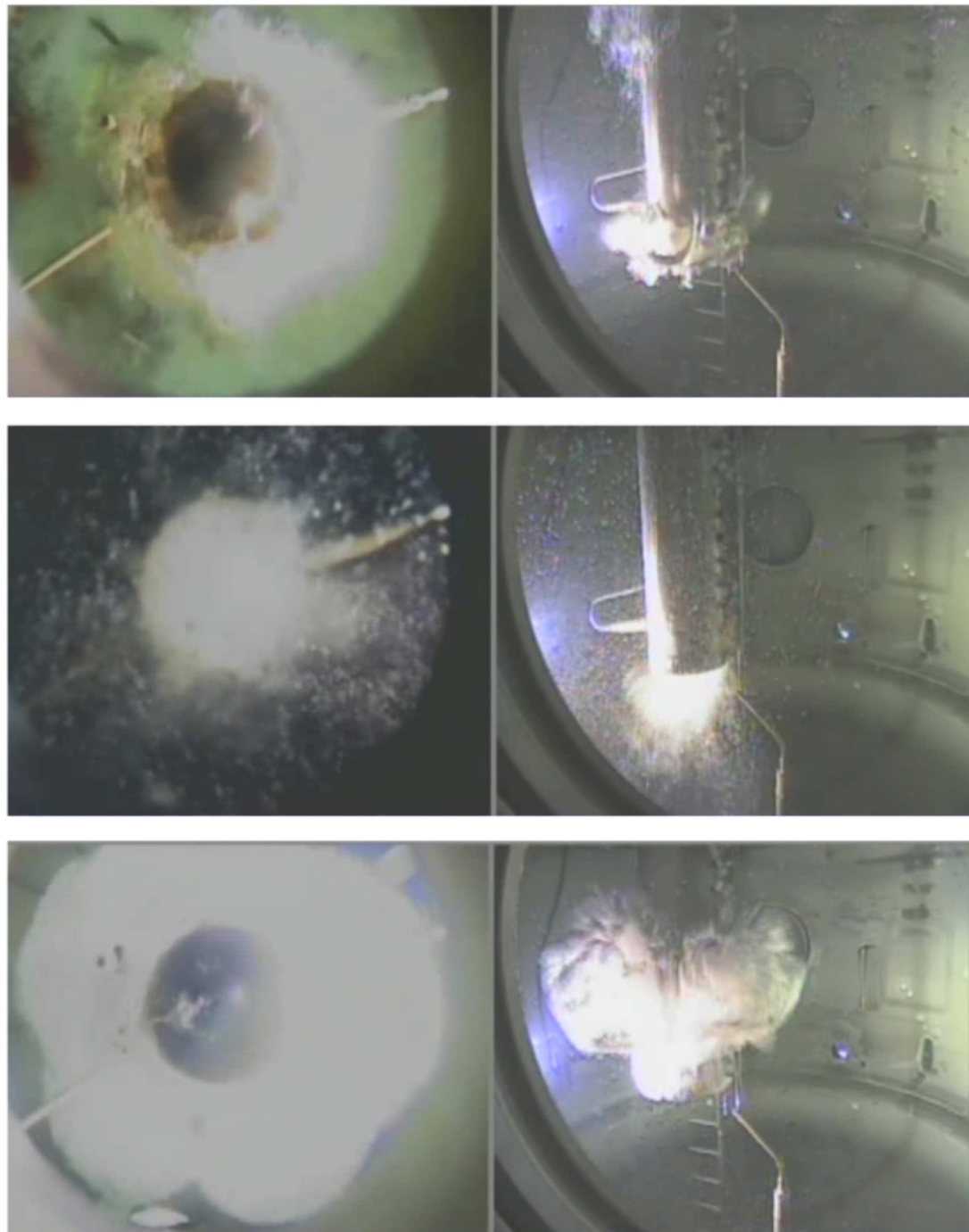


Figure 3.2. Different bubble modes. Air/steam mixture in MIX-01 (the uppermost image), jet in MIX-02 (center), and mushroom-type steam bubble in MIX-03 (the lowest image).

4 Introduction to Image Processing and Pattern Recognition Using MATLAB

MATLAB (Matrix Laboratory) is a numerical computing environment developed by Mathworks, Inc [22]. As the preliminary pattern recognition algorithm by Vesa Tanskanen was made by using MATLAB, and because MATLAB's Image Processing Toolbox is an efficient tool for image reconstruction and analysis [23], it was decided to continue the using of the same software in this thesis. Image Processing and Analysis in Java (ImageJ) program was the second option which was considered. ImageJ is a public domain Java image processing program, which is often used in medical applications [24]. ImageJ works with MATLAB, but it did not have anything extra compared to MATLAB's Image Processing Toolbox, therefore, MATLAB was chosen instead.

4.1 Digital Image Representation

A two-dimensional RGB image, sometimes called a truecolor image, is stored in MATLAB as an $M \times N \times 3$ matrix, where M is the number of rows, N is the number of columns, and each pixel is specified by three values — red, green, and blue — in the third dimension. When an RGB image is converted into a grayscale image of spatial size $M \times N$, each pixel may be presented by a function $f(x, y)$, where (x, y) is the location of a pixel whose brightness is given by the function $f(x, y)$. The brightness values of $f(x, y)$ are digitized with a specific resolution such as 8-bit (256 shades of gray), 12-bit (4096 shades of gray), or more. The

2-D grayscale image may be presented as a matrix I such as

$$I = \begin{pmatrix} f(1,1) & f(1,2) & \dots & f(1,N) \\ f(2,1) & f(2,2) & \dots & \vdots \\ \vdots & \vdots & \ddots & \vdots \\ f(M,1) & \dots & \dots & f(M,N) \end{pmatrix}. \quad (4.1)$$

All actions made by MATLAB will change the values of the elements of the matrix I depending on the performed operation. In an 8-bit grayscale image, the intensity values of the matrix elements vary from 0 to 255. If the image is underexposed, or in other words, the image looks too dark, too few shades of gray have been used. For example, the values of shades of gray in an 8-bit image might be between 0 and 100. `Imadjust` function can be used to spread the shades of gray level linearly to the full range of variation. Thus, the intensity values of the matrix elements are spread to the full range of variation from 0 to 255.

The grayscale image converted into a binary image, i.e. black and white, is presented as a similar matrix BW; function $f(x,y)$ values are 1's or 0's. An appropriate threshold can be found automatically by using `graythresh` function for the conversion. The binary image is stored to MATLAB as a logical array.

4.2 Basic Operation with Image Processing Toolbox

The basic matrix operations such as dividing, subtracting, adding, and multiplying can be made to an image matrix with `imdivide`, `imsubtract`, `imadd` and `immultiply` functions. `Z = imdivide(X,Y)` divides each element in the array X by the corresponding element in array Y and returns the result in the corresponding element of the output array Z. Similarly, `Z = immultiply(X,Y)` multiplies each element of X by the corresponding element of Y and returns the product in the corresponding element of Z. `Z = imsubtract(X,Y)` subtracts each element of Y from the corresponding element of X and returns the difference in the equivalent element of Z. The absolute difference between the corresponding elements of X and Y can be found with a function `Z = imabsdiff(X,Y)`. `Z = imadd(X,Y)` adds each element of X with the corresponding element of Y as expected.

4.2.1 Image Reconstruction

Grayscale and RGB images may contain noisy spots, dots, and larger zones with more striking colors or brighter shades of gray than the other parts of the image. It is worth removing these zones because they tend to cause errors to the pattern recognition results. These areas are the so called regions of interest (ROIs). For the removing of an object or filtering ROIs, the `roifill` and `roifilt2` functions are used. `Roifill` function fills the ROI by interpolating the pixel values from the borders of the region. If perfectly placed, the `roifill` function may work better than the real intensity adjustment functions. `Roifill` function is also useful for removing the extraneous details or artifacts.

The `roifilt2` function is an example of an intensity adjustment function. The `roifilt2` function applies a filter to a region of an image, where a binary mask defines the region. The function needs a filter to be defined. A useful filter is for example the `brighten` filter, which increases or decreases the color intensities in a colormap by replacing the current colormap with a brighter or darker colormap of essentially the same colors.

Image contrast adjustment is possible with `imadjust` function. Basic function `J = imadjust(I)` maps the intensity values of grayscale image `I` to new values in `J` in such a way that 1% of data is saturated at low and high intensities of `I`. Also the `decorrstretch` function which applies a contrast following the decorrelation stretch can be used. It is worthwhile to do all necessary operations to grayscale images before converting the images to binary.

4.2.2 Pattern Recognition and Image Analysis

The Image Processing Toolbox includes many operable functions for pattern recognition and image analysis. After a suitable binary image has been found, the matrix contains only 1s (white pixels) and 0s (black pixels). Tracing the boundaries of the white regions of the image, the `[B L] = bwboundaries(BW, 'noholes')` function can be used. The function traces the region boundaries in the binary image and returns the label matrix `L` as a secondary output. All white objects and holes in the picture are labeled. `L` is a two-dimensional array of non-negative integers that represent continuous regions. Option `'noholes'` searches only for object boundaries. Typical label matrix `L` can be presented as an arbi-

trary 10×10 matrix L

$$L = \begin{pmatrix} 1 & 1 & 0 & 0 & 0 & 0 & 0 & 0 & 0 & 5 \\ 1 & 1 & 0 & 2 & 2 & 0 & 0 & 0 & 0 & 0 \\ 1 & 1 & 0 & 2 & 2 & 0 & 0 & 0 & 0 & 0 \\ 1 & 1 & 0 & 0 & 0 & 0 & 3 & 0 & 0 & 0 \\ 1 & 1 & 0 & 0 & 0 & 3 & 3 & 3 & 0 & 0 \\ 1 & 1 & 0 & 0 & 0 & 0 & 3 & 0 & 0 & 0 \\ 1 & 1 & 0 & 0 & 0 & 0 & 0 & 4 & 4 & 4 \\ 1 & 1 & 0 & 0 & 0 & 0 & 0 & 0 & 4 & 4 \\ 1 & 1 & 0 & 0 & 0 & 4 & 4 & 4 & 4 & 0 \\ 1 & 1 & 0 & 0 & 0 & 4 & 4 & 4 & 0 & 0 \end{pmatrix}. \quad (4.2)$$

The label matrix L is also shown in Figure 4.1 as an image.

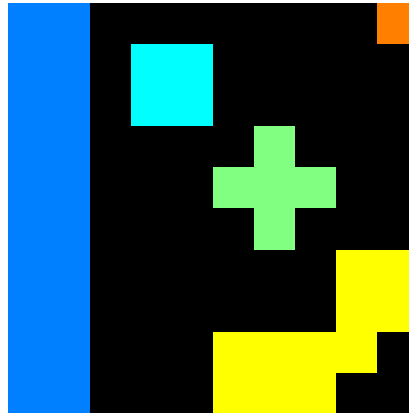


Figure 4.1. Label matrix L as an image. Black areas are the elements of matrix containing zeros and colored areas are labeled regions.

After the boundaries of the bubbles have been found, the properties of the labeled regions can be measured. The `regionprops` function is able to measure many different properties of the image regions. `STATS = regionprops(L, properties)` measures a set of properties for each labeled region L. L can be a label matrix measured with `bwboudaries`, with `bwlabel` or other multidimensional array.

When L is a label matrix, positive integer elements of L correspond to different regions. The set of elements of L equal to 1 corresponds to region 1, the set of elements equal to 2 corresponds to region 2, and so on. An arbitrary label matrix L in Equation (4.2) consists of 5 different regions labeled from 1 to 5.

Different measurements can be made for each region as specified by string **properties**. Properties can be split to shape measurements and pixel value measurements. The latter works only with grayscale images.

Over twenty different shape measurements can be made. The area measurement calculates the actual number of pixels in the region. The area of the bubble profile can be measured with '**Area**' property. The center of the mass of the bubble profile can be measured with string '**Centroid**'.

'**Eccentricity**' might be useful with steam bubbles. It specifies the eccentricity of the ellipse that has the same second-moments as the region. The eccentricity is the ratio of the distance between the foci of the ellipse and its major axis length. The value is between 0 and 1.

'**EquivDiameter**' is the property that specifies the diameter of a circle with the same area as the region. '**MajorAxisLength**' specifies the length of the major axis of the ellipse that has the same normalized second central moments as the region. The length is measured in pixels. Similarly, it is possible to calculate minor axis length with the string '**MinorAxisLength**'.

Sometimes it might be valuable to know the pixel values of the bubbles. Desired pixel values can be listed with '**PixelIdxList**' and '**PixelList**' strings.

The results of the measurements can be presented by diagrams, graphs, charts or with other visualisation methods depending on the users' needs.

5 Pattern Recognition Algorithm

The developed algorithm consists of two parts: pattern recognition of the bubbles and analysis of the recognized bubble images. In this chapter, the pattern recognition of the bubbles is described in detail. The analysis of the recognized bubble images will be introduced in Chapter 6.

5.1 From Recorded Video to Image Sequence

An AVI videotape recorded during the experiments was converted to JPG image sequence using free Audio Video to Picture converter software [25]. Each frame had a horizontal resolution of 720 pixels and a vertical resolution of 576 pixels and was made up of a quartet of zones as shown in Figure 5.1. The blowdown pipe outlet in the wet well in the upper left corner of the picture was shot with a high speed camera. The dry well compartment in the upper right corner was shot with normal speed camera, as well as the bottom of the pipe's outlet in the lower left corner and pipe's profile in the lower right corner of the frame.

Due to the recording process of the video, it was not possible to use the high speed mode of the high speed camera at the same time with three normal speed cameras. The cassette recorder records all four parts of the picture at the same time, and thus, different framerates between the cameras were not allowed. Hence, all cameras were in the normal speed mode of 25 fps. The high speed camera was zoomed in on the pipe's outlet so near, that bubbles did not fit into the picture and the upper left corners of the images were thrown aside, except some editing was made. In terms of bubble recognition, the dry well compartment was uninteresting, because there were no bubbles and the upper right corner of the picture was ignored. Only the lower pair of the frames was used in the algorithm.



Figure 5.1. Reference image

5.2 Structure of the Pattern Recognition Algorithm

The algorithm was made with the idea that if the background is removed from the image, only bubbles of interest remain. A simplified flow diagram of the pattern recognition algorithm is presented in Figure 5.2. The MATLAB code is not included in this thesis, but is available from the author on request.

In the algorithm, an empty background image without bubbles was used as a reference image. Due to the different shutter speeds of the cameras and lighting differences between the shooting directions, a new reference image had to be chosen every time. The algorithm started by choosing this reference image. The image was converted from an RGB image to grayscale. It was impossible to make an algorithm which would work with every single frame due to different bubble types. For this reason, a decision was made to use a shorter part of the videos with uniform bubble types. It could be possible to do this kind of a bubble type selector for example by using a subloop which will look the bubble, guesses the bubble type, and returns back to make a better inspection.

After choosing the reference image, a suitable bubble type was selected. Three typical bubble types occurred: steam, air, and jet.

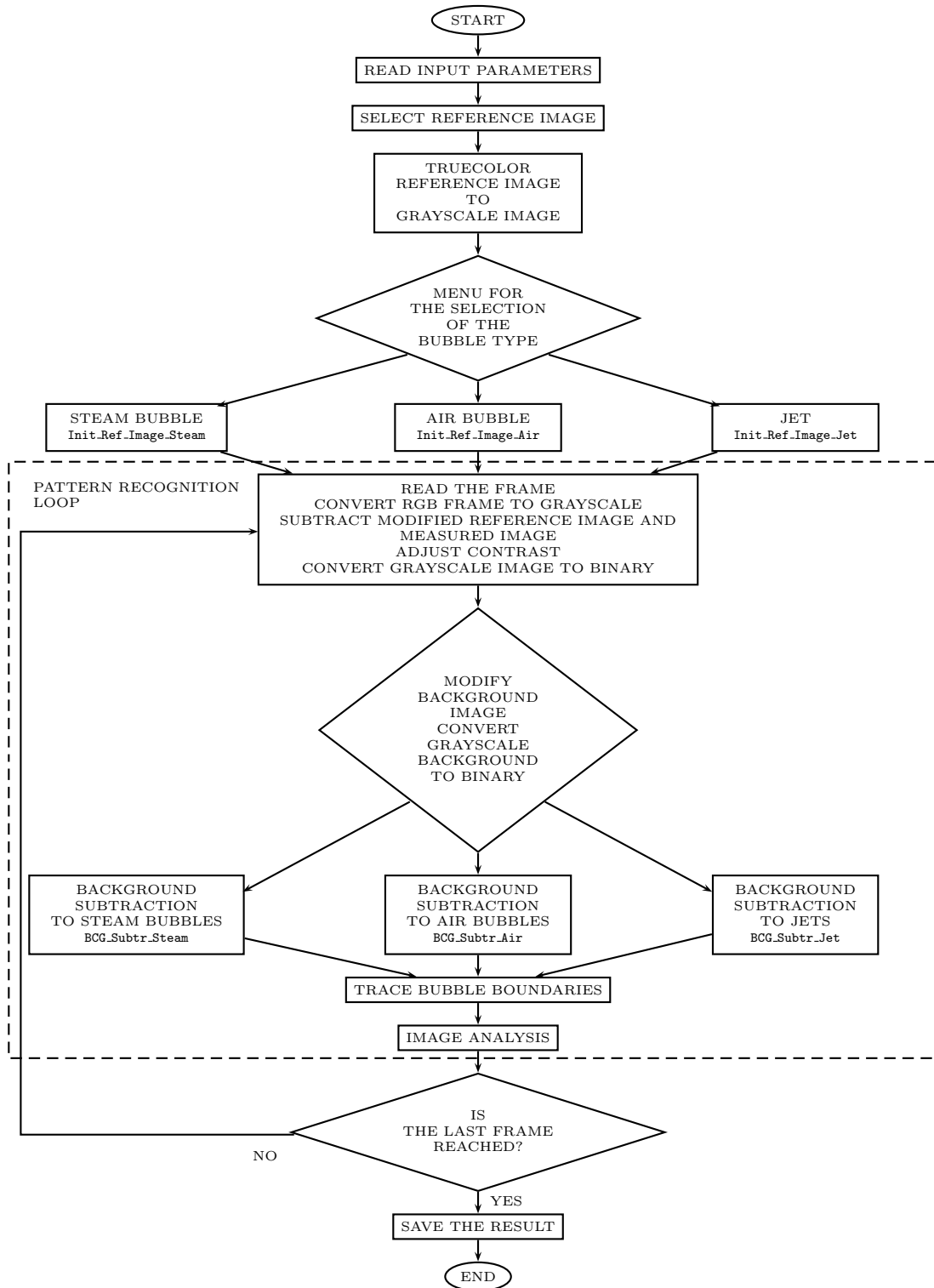


Figure 5.2. Simplified flow diagram of the pattern recognition algorithm.

5.2.1 Init_Ref_Image_(Steam/Air/Jet) functions

As noticed in Figure 5.1, images contained many overexposed regions and disruptive extraneous details. These exposure problems were adjusted, and additional details were removed. All filtered regions of interest (ROIs) are shown in Figure 5.3.



Figure 5.3. Filtered regions of interest.

Different filtering operations from A to P were made by `Init_Ref_Image_(Air-/Steam/Jet)` functions depending on the selected bubble type. In the case of mushroom-like steam bubbles, all actions between A and P were made.

In the upper left corner of the image, the biggest problem of the high speed camera frames was the overexposed reflection of the pipe wall, marked as A in Figure 5.3. The overexposure was equalized with a ROI mask polygon by the `roifill` function. Region A was the only modified part of the high speed camera frame.

In zone B, the pressure transducer made an overexposure-like reflection in the middle of the lower left corner picture. Both the `roifilt2` and `roifill` functions were tested, and the latter worked better. The reflection of the fastenings of the ladder at point C was darkened with the `roifill` function.

White boxes, enclosures etc. may cause illusion of bubbles when converting gray-

scale image to binary. Therefore, a square box D of the right corner of the lower left picture was filled with the **roifill** function.

The obtrusive print on the top of the wet well ceiling E and white enclosure F at the bottom of the picture were also darkened with the **roifill** function.

The mouth of the pipe G was not a disruptive object, but on account of lighting a black circle appeared during the conversion of the image type. The **roifill** function was used to interpolate the blowdown pipe's outlet.

Zones H and I were darker than the rest of the picture. Both domains were lit up with the **roifilt2** function with the **brighten** filter, followed by the smoothing of the lighting with the **roifill** function.

Due to the variable lighting, the lower left corner remained dusky. At the point J, the whole lower corner was lit up at the level of 0.08 of the **brighten** filter. The precise value of the **brighten** filter was hard to find and even the level of 0.01 difference of brighten value may misdirect the whole operation in the wrong direction.

A smaller circle, the chain link of the second blowdown pipe K, brought on similar lighting problems as the blowdown pipe's outlet, and it was treated like the blowdown pipe G with the **roifill** function. Between the smaller reflection of the fastenings of the ladder and the chain link of the second blowdown pipe, there was a triangular area L which was darker than the other parts. An exact position of polygon mask was difficult to discover, but it succeeded with the **roifilt2** function and the **brighten** filter.

The film shot from underneath the pool was the most difficult to deal with due to the large amount of disruptive objects and unhomogeneous lighting. There were also zones in the picture where modifications were beyond all reason, but were resolved anyway.

The blowdown pipe's profile in the lower right corner of the picture consisted only of a few difficult areas. The left side of the pipe was overexposed, and the right side of the pipe was, vice versa, underexposed. It was possible to fix the overexposure with two consecutive operations at the points M and N with consecutive **roifilt2** and **roifill** functions and the **brighten** filter. Underexposed right side of the pipe was left untouched.

Bright light coming from the left side window was reflected disruptively from the ladder on the right side of the pipe. Reflections looked harmless, but due to the

uneven lighting, bubbles were split into several parts which caused incorrect pattern recognition results. The `roifill` function was applied to remove reflections at the point O.

The last big problem with the frames was the dark top part of the picture. Particularly, the downside of the blowdown pipe remained so dark that a part of the bubble vanished into the background. At the area P, a large rectangle of the topmost part of the picture was brighten with the `roifilt2` function.

All above actions from A to P were used with mushroom-type steam bubbles as mentioned. The result image of actions A to P is shown in Figure 5.4.

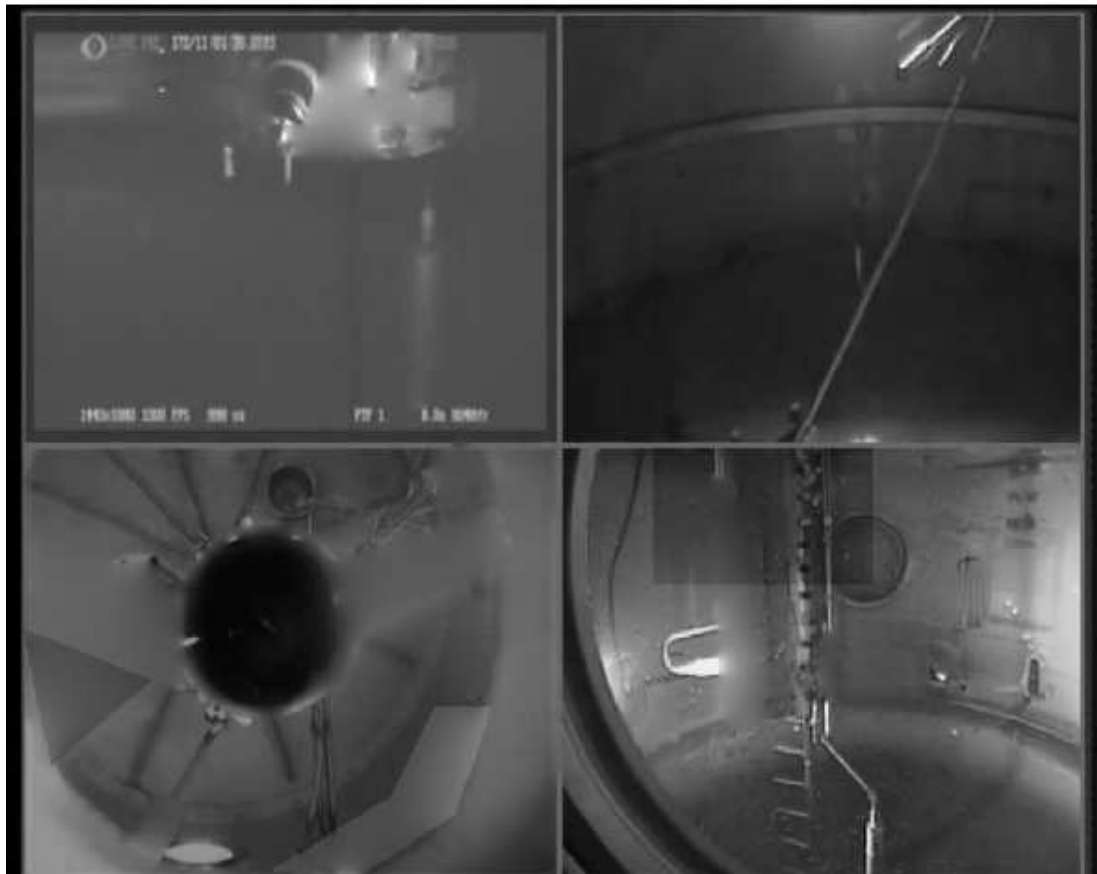


Figure 5.4. Result image of actions A to P.

To jets and air bubbles only a portion of actions were used. In Appendix III, the actions used in `Init_Ref_Image_Air` and `Init_Ref_Image_Jet` functions are shown in flow diagrams. For example, the jets did not rise over the pipe's outlet, and therefore, the overexposed reflection on the left side of the pipe did not have to be removed.

5.2.2 Pattern Recognition Loop

At the beginning of the pattern recognition loop, in order to compare measurements and recognized images, the indexes of images were converted to time values by `get_image_number` function and framerate. The first RGB frame of image sequence was read and converted to a grayscale image. The modified reference image was subtracted from the image of interest by using `imsubtract` function. Most of the disruptive details were removed in the subtraction. After the subtraction, the image was darker than before. The contrast of the upper left corner and lower right corner of the image was adjusted with `imadjust` function. `Decorrstretch` function was used to apply the decorrelation stretch to the lower left corner of the image, and then to increase the contrast.

The brightened image was converted to binary using the `graythresh` function that uses the Otsu's method which chooses the threshold to minimize the intra-class variance of the black and white pixels [26].

The background image `Lbcg` was constructed by subtracting the modified reference image from the original reference image. Same contrast adjustments were made to the computed image. After this, the background image was converted to binary.

Because the binary image contains only 1s and 0s, it was possible that during the subtraction of the binary background image and computed image, some valuable information was lost. For example, the subtracting of the white reflection of the pipe from the mushroom-type bubble caused a large hole in the middle of the bubble. In `BCG_Subtr_(Steam/Air/Jet)` functions, these possibilities were attempted to be removed with multiple if-else statements. The number of statements depended on the selected bubble type.

As the best compromises were made with if-else statements, the `bwboundaries` function was used to trace the boundaries of the bubbles. `Bwboundaries` function returned also a label matrix `L` as the second output argument. `L` is a two-dimensional array of non-negative integers that represent contiguous regions. The label matrix `L` was used in the image analysis.

6 Image Analysis

After the pattern recognition was done and the edges of the bubbles were found, the information about the bubbles was collected. The matrix L was obtained by using `bwboundaries`, and to be on the safe side, the matrix L was converted to a real label matrix by using `labelmatrix = bwlabel(L)` function. All the interesting information in the images was at the lower part of the pictures. The `labelmatrix` was divided into two parts: the lower left part `label_bottom = labelmatrix(downrow, leftcol)` shot from the bottom of the pool and the lower right part `label_profile = labelmatrix(downrow, rightcol)` showing the profile image of the blowdown pipe. The uninteresting upper part of the pictures was ignored. From now on, the `bottom` and `profile` refer to the lower left and lower right part of the picture, respectively.

The centers of mass and the areas of the bubbles in pixels were calculated with the functions `STATS1 = regionprops(Label_bottom, 'Area', 'Centroid')` and `STATS2 = regionprops(Label_profile, 'Area', 'Centroid')`. The width and height of one pixel in centimeters vary, due to the position of the camera, the angle of the camera, and the refractive index of the content of the pool. The size of a pixel in centimeters was measured by using a reference ellipse fitted on the pipe's outlet. Because the `profile` picture was shot downwards to the pipe's outlet and an ellipse figure of the outlet cannot be seen, the ellipse was fitted in the pipe's outlet manually, on both the `profile` and `bottom` picture. Fitting the ellipse to the `profile` picture may cause some errors to the evaluation of the height of a pixel.

An ellipse with the width of approximately 115 pixels and height of 120 pixels was fitted to the `bottom` picture. The diameter of the DN200 pipe is 219.1 mm, and therefore, the width of one pixel `Pixel_width_bottom` and height of one pixel `Pixel_height_bottom` in the `bottom` picture was calculated.

Fitting the ellipse to the `profile` picture was more complicated due to the lack of

resolution, because the edge of the pipe was hard to find. The angle of the camera was approximately known, and an ellipse was fitted. The height of the ellipse was approximately 15 pixels, and the width of the ellipse was approximately 45 pixels. The width of one pixel in the `profile` picture `Pixel_width_profile` was calculated similarly as in the `bottom` picture. If the pipe's outlet was viewed at the same level, only a straight line would have been seen. When looking downwards, the length of the pipe will look shorter than it is [27, 28], as shown in Figure 6.1.

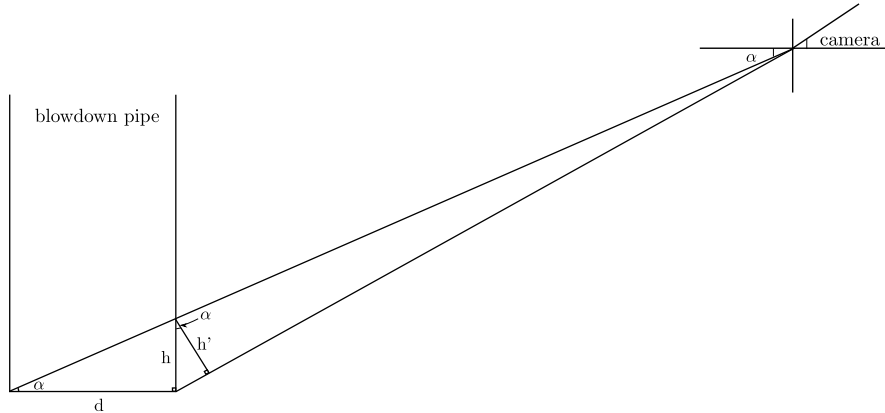


Figure 6.1. Correction to the image due to camera position. d is the diameter of the pipe, h is the height of the pipe section, h' is the height of the pipe section seen in the image, and α is the angle of the camera.

The camera was tilted at an angle α . The height of the pipe which was seen is h' , and the real height of the pipe is h . The diameter of the pipe is d . All the angles α in Figure 6.1 are the same due to the geometry, if the rays from pipe to camera are assumed parallel. From the similar triangles

$$\frac{h'}{h} = \frac{d}{\sqrt{h^2 + d^2}} \quad (6.1)$$

$$h = \frac{dh'}{\sqrt{d^2 - h'^2}} \quad (6.2)$$

In the algorithm, d is `Fitted_ellipse_width_profile`, h' is `Fitted_ellipse_height_profile` and h is `Bubble_height_profile`.

Also, the refractive index of the pool content affects the magnification of the image and it should be taken into account [29]. With an empty pool, the content is air and the refractive index $n_a = 1.00$. The refractive index of water, `Refractive_index_of_water_n_w`, is $n_w = 1.33$. In Figure 6.2, the influence of water to the magnification is described in detail.

The diagram presents a simplified version of the camera, with the refracting surface of radius R , which focuses the light rays from an object of height h onto a

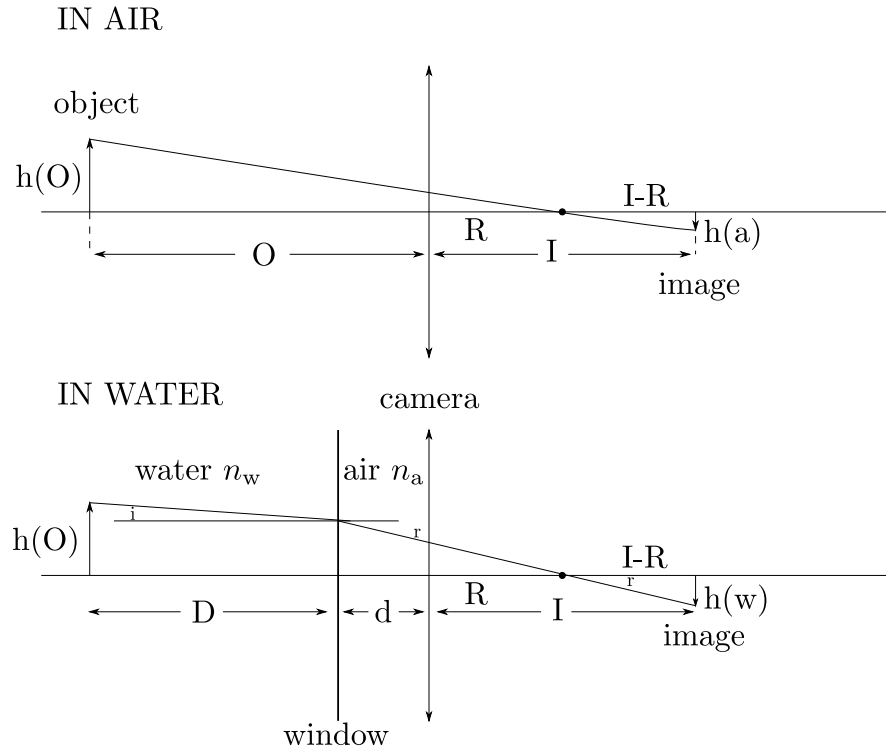


Figure 6.2. Image magnification due to the pool content.

distance I from the camera lens surface. The real camera contains a lens system which is now approximated by one lens. In air, the usual result of ray optics can be seen. By similar triangles, the height of the image $h(a)$ is

$$h(a) = h \frac{I - R}{O + R}. \quad (6.3)$$

For the same relative positions of object and camera, but with the object in water and the camera in air behind a water-air interface, the configuration is shown in the lower part of Figure 6.2. An incident angle of refraction at the window is i and the angle of refraction from the window is r . The height of the image $h(w)$ is now

$$h(w) = (I - R) \tan(r). \quad (6.4)$$

Using similar triangles again, the object height h can be presented as

$$h = D \tan(i) + (d + R) \tan(r). \quad (6.5)$$

Inserting Equation (6.5) into Equation (6.3), and then using Equation (6.4), we

get the ratio

$$\frac{h(w)}{h(a)} = \frac{O + R}{D_{\tan(r)}^{\tan(i)} + (d + R)} \quad (6.6)$$

The refraction at the window can be described mathematically by Snell's Law,

$$n_w \sin(i) = n_a \sin(r). \quad (6.7)$$

The approximation that the window is thin and not taken into account in the calculations was made. For small angles the sines and tangents of angles are approximately the same, and thus, it can be assumed that

$$n_w \tan(i) = n_a \tan(r) \quad (6.8)$$

$$\frac{\tan(i)}{\tan(r)} = \frac{n_a}{n_w}. \quad (6.9)$$

Inserting this into Equation (6.6) and noting that $O = D + d$, one can get the image magnification

$$M = \frac{h(w)}{h(a)} = \frac{D + d + R}{D \frac{n_a}{n_w} + (d + R)}. \quad (6.10)$$

At the PPOOLEX test facility, the camera was fixed outside of the pool a couple of centimeters away from the window. The distance between the pipe and the window was approximately $D \approx 143$ cm, calculated from Figure 2.3. The largest possible magnification that can be produced by a planar water-air interface is the same as the refractive index of the water. The radius R of the camera was not known, and therefore, the approximation $R = 0$ cm was used. With these values, the magnification caused by water was $M = 1.3239$. With the calculated magnification, the height of the pixel `Pixel_height_profile` was evaluated. All the areas in pixels were converted to square centimeters.

The cross sectional area of the bubble and the profile area of the bubble were measured with the `regionprops` function. The area of the bubble was presented in square centimeters. The cross sectional area of the bubble was used to determine the average value of the bubble diameter. The largest bubbles did not fit into the picture shot from the bottom of the pool, and some of the information was lost. Due to this limited bubble diameter from the `bottom` camera, the diameter was not estimated in the same direction as in the `profile` picture. Comparable information about the bubble diameters was also lost with the largest bubbles. The

largest diameter of the bubble in the horizontal direction, shot from the bottom of the pool, was measured and compared with the biggest diameter of the bubble in the profile picture. From the profile picture, both the maximum bubble width `Bubble_width_profile_centimetresquared` and height `Bubble_height_profile_centimetresquared` were estimated.

There might be several different ways to calculate the chugging frequency. The pixel value comparison method was used in this study. For all bubble types, a comparison rectangle was chosen. The positions of the rectangles are presented in Figure 6.3. The yellow, red, and green rectangles are the ratio boxes for jet, steam, and air bubbles, respectively. The number of nonzero elements (white pixels) in the box was measured and compared to the whole amount of pixels in the rectangle. The chugging frequency was calculated by taking the fast Fourier transform (FFT) from the ratio of the pixels. The chugging frequencies should appear into the FFT with large frequency spikes.

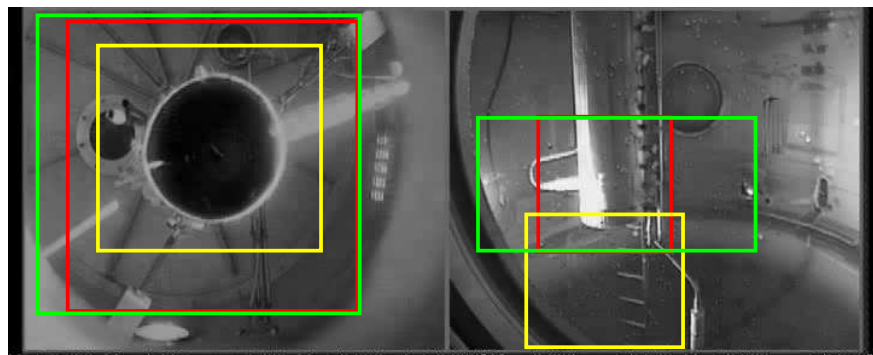


Figure 6.3. Rectangles used in the chugging frequency calculations. The yellow rectangles are for jets, the red rectangles are for air bubbles, and the green rectangles are for steam bubbles.

7 Results and Discussion

In this chapter, the results of the pattern recognition and the image analysis are presented, such as feasibility of the pattern recognition algorithm.

7.1 Results of the Pattern Recognition

The functionality of the pattern recognition algorithm was tested with multiple bubble types. Series of 25 images, in other words a time period of 1 s in the video, of each bubble type are presented in Appendix IV for air bubbles, in Appendix V for steam bubbles, and in Appendix VI for jets.

For air bubbles, the downside of the pipe creates quite a lot of errors with lost information. On the bright side of the pipe, the recognition works well and the recognized bubbles appear the same as the original bubbles. The image shot from the bottom of the pipe looks dark, but despite that, only a little information is missing. Unfortunately, air blow down is not very interesting of the scientific point of view, and it appears only at the beginning of the measurements.

The mushroom-type steam bubbles are recognized well in the `profile` picture as can be seen in Appendix V. A part of the bubble is missing on the darker upper side of the bubble, but the form of the bubble is captured well. Also the formation of a new bubble can be easily seen. When the bubble has risen in the middle of the pipe, a part of the reflection of the pipe is calculated incorrectly to the area of the bubble. The incorrect area will get lost with a large amount of data. However, larger errors are produced with the `bottom` camera. During the formation of the bubble, the reflective parts of the instrumentation made the recognition of the boundaries more difficult. The early phase of the bubble remains dispersed, and the real shape of the bubble is difficult to detect. Some modifications to this part of the algorithm have to be done in the future. For

more inflated larger bubbles, the recognition from the `bottom` camera picture works well, and only a little information is lost.

Due to the lack of resolution of the images, the recognition of jets was the hardest part to get functional. As shown in Appendix VI, the areas of the jets in the `profile` picture are larger than the real areas in the grayscale images. Sometimes when there is not even a jet in the real image, the algorithm sees one. The swarms of bubbles produced by the jets made the water look noisy, and the background looked brighter than it really was. A few corrections of this lighting problem could be tried in the future. Eventhough the `profile` area was too large, the `bottom` camera helped a lot. The cross section of the jet was recognized better and information is neither lost nor artificial information produced.

The video framerate of the experiment was only 25 fps. The formation frequency of the jets is so fast that it is possible that some break up and formation of the jets might occur between two images. Therefore, within two consecutive images, there can be two different jets looking like each other. The former jet's break up and the new jet's formation was lost between these two images.

If a jet will appear without other bubble types present, the recognition procedure does not make much errors. Problems may arise if a jet appears in the middle of other bubble type recognized. To the jet type bubbles, nothing was done concerning the reflections of the pipe. If the steam or air bubble mode was selected and a jet appeared, the reflection of the pipe was cut off. An improved selection method should be planned in the future. In the MIX-01, MIX-02, and MIX-03 videos, this kind of mixed bubble mode did not occur, and the selection method was not considered.

In the real situation, an immeasurable amount of bubble modes will appear. Most of the measurements are unpredictable, and a lot of work is demanded to make a perfect pattern recognition algorithm. In medical experiments, such as retinal inspection, the inspected object, the eye, remains similar. Most of the defects are results from some mutation. In other words, the difference between two images reveals the problem areas quite clearly [30, 31].

When water is blowed to a pool like the PPOOLEX test vessel, the developed bubble mode will be quite unpredictable, depending on many different reasons, such as the temperature of the water, the mass flow rate of the steam, the temperature of the wet well, and so on. Many different bubble modes exist, and the fluctuation between the modes is fast. Small swarms of bubbles can appear at any time and blur the water making the lighting of the pool change suddenly.

Some of the swarms are disruptive, some are not. Sometimes the instrumentation inside the pool has to be changed causing a need to modify the pattern recognition procedure.

7.2 Results of the Image Analysis

Compared to the preliminary pattern recognition procedure [12], the extra camera at the bottom of the pool was used. This feature was utilized also in the image analysis. The maximum diameter of the bubble was measured with all bubble types from the `profile` picture. Similarly, the horizontal maximum diameter was evaluated from the `bottom` picture. The diameter could not be measured in the same direction, because the largest bubbles did not fit into the `bottom` picture. The maximum calculated diameters in the `profile` and `bottom` pictures are shown in Figure 7.1.

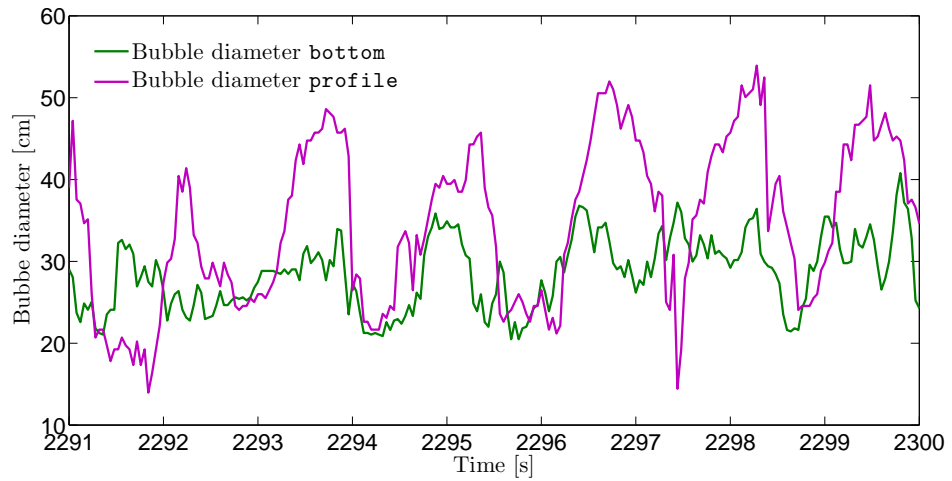


Figure 7.1. Maximum diameter of the jet in the picture shot from the `bottom` of the pool and maximum diameter of the jet in the `profile` picture.

As can be seen, the maximum diameter of the jet is very realistic in the `bottom` picture, but the maximum diameter shot from the `profile` picture is too large due to errors in the pattern recognition procedure. However, these two different measurements support each other quite well.

There was no use to measure the three-dimensional quantities from these two-dimensional pictures due to several sources of errors. For jets with a circular cross section, the volume was measured by using the height of the bubble from the `profile` picture and the surface area of the bubble from the `bottom` picture. Otherwise, the three-dimensional calculations were left for the future.

As a test, a three-dimensional solid of revolution was made by using a two-dimensional label matrix L. From the label matrix, only the lower right side of the picture was taken. The central axis of the pipe was defined as the axis of revolution. The result of the rotation is shown in Figure 7.2. The obtained object is full of approximations, and thus, many problems appeared. The bubble is very seldom symmetrical. Should the left or right profile rotate the full circle or should the left and right profiles be rotated a half circle separately? The borders will never meet; how to solve this? There will always be steps on the edge. Comparing the solid of revolution, the original image and the label matrix of the bubble showed in Figure 7.2, it can be seen that there is something similar between the 3D image and the original bubble, but it does not look reliable from a scientific point of view.

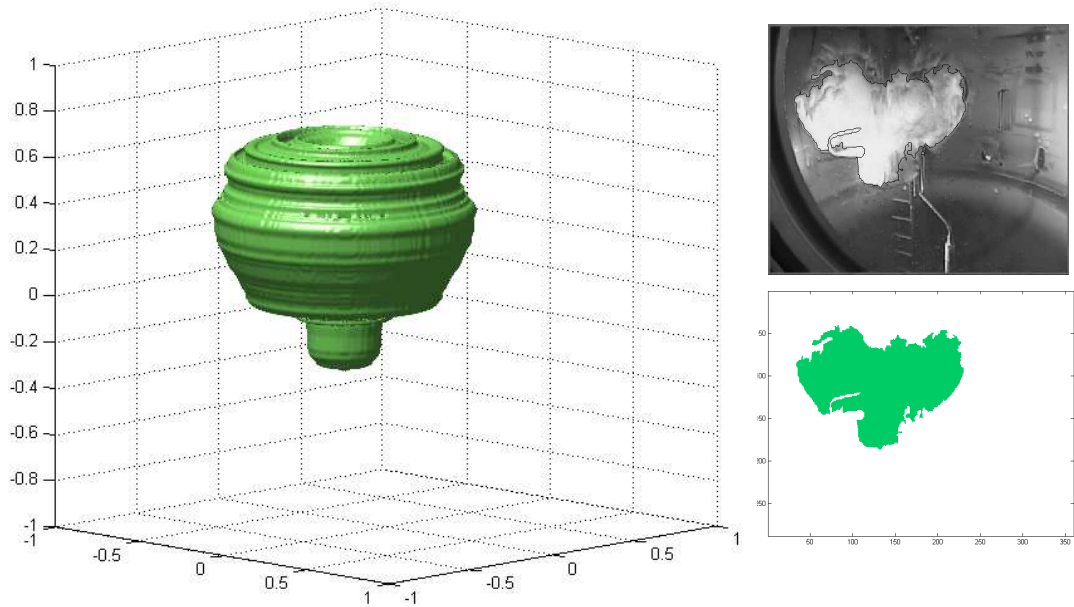


Figure 7.2. A three-dimensional "bubble" made from the two-dimensional image, the profile image, and the original grayscale image.

7.3 Calculation of the Chugging Frequency

The chugging frequency was calculated by using the ratio rectangles described in the previous chapter. In all the MIX experiments, the oscillation frequencies were measured inside the blowdown pipe during a ten seconds period. For all experiment videos, the chugging frequencies were evaluated by using the same time period. The jet bubble mode was used. The white pixels of the rectangle

were compared to the whole amount of pixels in the rectangle. The `Bubble_ratio` data was transformed by FFT, and the chugging frequencies were measured from the FFT figures. The `Bubble_ratio` calculation in MIX-03 experiment is shown in Figure 7.3. The FFT figures of all experiments MIX-01, MIX-02, and MIX-03 are shown in Figures 7.4, 7.5, and 7.6.

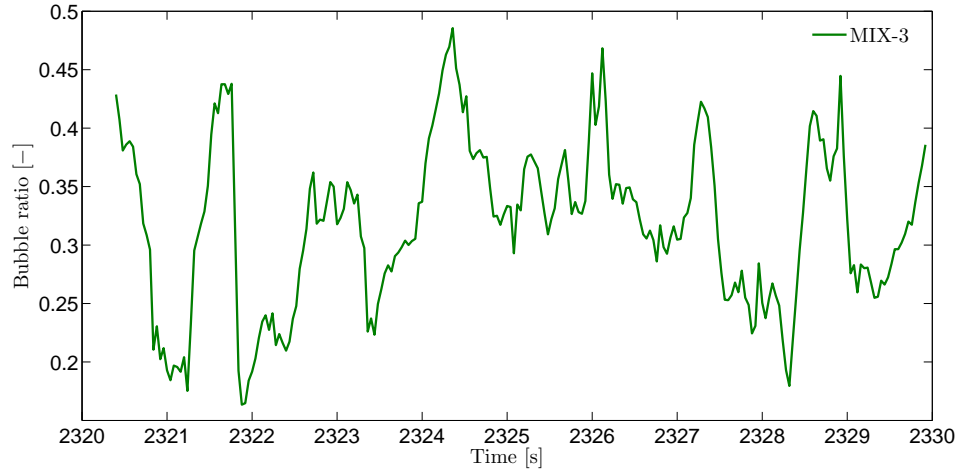


Figure 7.3. Area of the white pixels compared to the whole area of the comparison rectangle in MIX-3.

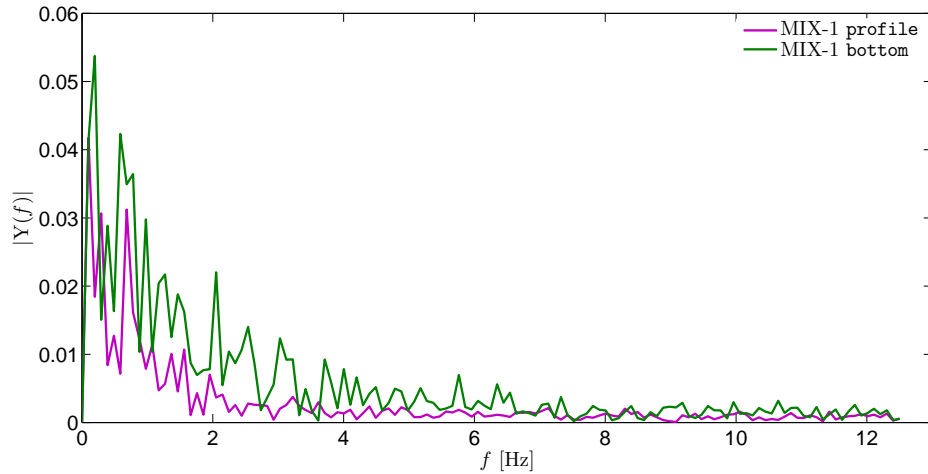


Figure 7.4. FFT produced from both the `bottom` and `profile` images in MIX-1.

The MIX-01 experiment video was quite a lot overexposed, and the pattern recognition procedure did not work very well with the `profile` picture. The chugging frequency was calculated both from the `profile` picture and from the `bottom` picture in order to achieve better precision. For MIX-02 and MIX-03 experiments, only the `profile` frequency was calculated, but it is possible to calculate frequencies from both pictures with all different bubble modes. The evaluated chugging frequencies are listed in Table 7.1.

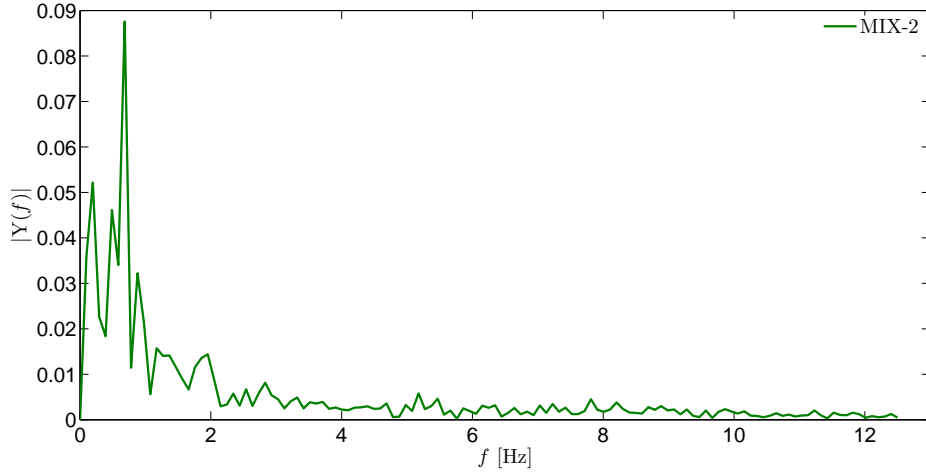


Figure 7.5. FFT produced from the profile picture in MIX-2.

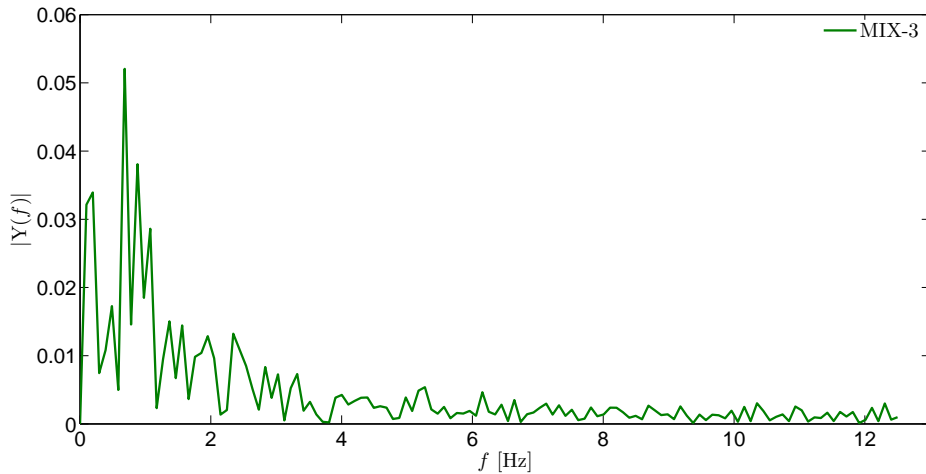


Figure 7.6. FFT produced from the profile picture in MIX-3.

Table 7.1. Measured oscillation frequencies and calculated chugging frequencies.

Experiment	MIX-01	MIX-02	MIX-03	Unit
Measured values				
Time period	2650.36–2659.96	2290.84–2299.90	2320.41–2329.90	s
Amplitude	29–668	268–999	100–668	mm
Average amplitude	318	533	493	mm
Frequency	0.80–1.56	0.77–1.06	0.60–1.23	Hz
Average frequency	0.99	0.90	0.90	Hz
Calculated chugging frequencies				
Largest frequencies in FFT	0.68, 1.07, 1.37 profile 0.59, 0.78 bottom	0.68, 0.88	0.68, 0.88, 1.07	Hz
				Hz

As can be seen, the chugging frequencies fit well between the oscillation frequencies. The chugging mode was also calculated by using steam and air bubble modes. The results were similar as measured with jets. The chugging frequencies

vary between 0.5–2.5 Hz, which are reasonable values.

7.4 Feasibility of the Pattern Recognition Algorithm

The pattern recognition algorithm was made by using videos from three similar measurements. The recorded video material consisted of images divided into four parts. Only the best two images were used. The algorithm should work well in the situations sufficiently similar as it has been prepared for. If any visible part of the test facility will be replaced or modified, some modifications to the algorithm should be done. The algorithm is suitable for the calculation of the chugging frequencies, even with poor pattern recognition and averaged diameters of the bubbles, but it should not be used for the bubble surface area or volume measurements. The maximum diameter of the bubble should be measured by using both the `bottom` and `profile` pictures. Neither will give a perfect value for the diameter, but together an approximation of the maximum diameter of the bubble is sufficient. However, the algorithm would be very useful when planning and carrying out the 3D pattern recognition algorithm in the future.

The algorithm works with one configuration, but it can be easily adaptable depending on different lighting modes, framerates, etc. For the future problems, the solutions will be easier to find with the help of the algorithm. The objective of this study was to improve the pattern recognition procedure. The improvements consisted of better removal of image background, more exact bubble boundary recognition, and more automated procedure. The pattern recognition procedure and boundary recognition were improved, but the automation of the procedure still needs some improvements.

8 Conclusions

During a possible loss of coolant accident in the Finnish type BWRs, a large amount of condensable steam will be released from the reactor pressure vessel to the suppression pool via blowdown pipes. Steam will be condensed on the dry well walls, inside the blowdown pipe, and into the suppression pool water causing dynamic and structural loads to the suppression pool. These loads can be measured with small scale test facilities by using thermocouples, pressure transducers, and strain gauges, but visually observable field data cannot be replaced by those measurements.

Nuclear Safety Research Unit at Lappeenranta University of Technology has done experimental suppression pool research over ten years with the POOLEX and PPOOLEX test facilities. In these experiments, the temperature, pressure, and strain gauge measurements were made both with an open pool and with a closed pressurised pool configuration. The durability of the pool is lawful, but was also tested in numerous experiments during various projects. Visual observation of recorded video material was used to evaluate the size, shape, formation and break up of the steam bubbles. The pattern recognition procedure was developed for single camera cases using the POOLEX data. The aim of this study, was to improve the preliminary pattern recognition algorithm for the dual camera cases.

In summer 2012, the thermal stratification and mixing experiments, MIX-01, MIX-02, and MIX-03, were made. With a large amount of video material, the experiments proved to be useful for constructing an improved pattern recognition algorithm. The algorithm consists of two parts. The first part is the pattern recognition of the bubbles, and the second part is an analysis of the recognized bubble images. The bubble recognition was performed with the three different bubble types: steam, air, and jet.

The recognition of the **profile** picture of the mushroom-type steam bubbles was successful, and only a little information was lost in the shadows of the blowdown

pipe. In the pictures shot from the bottom, under the blowdown pipe, larger errors of recognition appeared. During the formation of the bubble, the instrumentation in the pool caused complications in the observations, for example a part of the bubble could not be observed. Also the camera at the bottom of the pool was oriented in such a way that the full-sized bubble did not fit into the picture. Thus, a section of the bubble was cut off from the image.

For the blow down of air, the uneven lighting of the pool caused a large part of the bubble to disappear. Smoother lighting is required to improve the conditions. The recognition of the air bubbles by using the camera at the bottom of the pool succeeded well. Unfortunately, the pure air bubbles are uninteresting from a scientific point of view because the blowing of air will only happen at the beginning of the suppression pool experiments. If air bubbles will appear during more interesting bubble modes, the possible errors due to the air bubble recognition will disappeared into large amount of data.

Concerning jets, due to the low resolution of the images, the swarms of bubbles were recognized larger than they should have been. This problem would probably be resolved with higher resolution videos. Otherwise, the pattern recognition of jets worked well. Some misidentifications may occur if the jets appear during other bubble modes and the selected bubble mode is other than jet. Applying steam bubble mode to jets will create misrecognition due to the reflection of the left side of the blowdown pipe. The amount of such errors was impossible to test because in the video material of the MIX-01, MIX-02, and MIX-03 experiments, this kind of mixed modes did not occur.

The results of the bubble diameter and height measurements were reasonable. Some complications in the calculations were caused by geometrical optics, and some approximations have to be done in the measurement of the height of the bubble. The refractive index of water also affects the magnification of the image. Some approximations were made as the angle of the camera was not accurately known. The volume or the surface area of the bubble were not worth of analysing due to the fact that errors will build up to be huge when converting the 2D image to an artificial 3D image. One three-dimensional bubble was created for pure interest.

The chugging frequencies were calculated by using a reference rectangle to all bubble types in which the number of white pixels was compared to the whole amount of pixels in the rectangle and taking FFT of the pixel ratio. In the experiments, the oscillation frequencies were measured inside the pipe. These

results were compared to the pattern recognition results. The calculated chugging frequencies fitted well into the results. Even with the steam and air bubble modes the chugging frequency calculations turned out to be useful.

The pattern recognition algorithm should work well in the conditions it is designed for. If the measurement configuration will be changed, some modifications have to be done. Changing the resolution, turning the position of the cameras, or changing the image from four-part to one-part image will change the positions of the regions of interest. The structure of the pool is so complex that the pattern recognition algorithm which would work in all situations is unfeasible to implement unless the positions and angles of the cameras will be fixed. The created algorithm is however beneficial because even in the variable circumstances a practical solution will be found more easily. Numerous suggestions for improvement of the future 3D equipment were also found.

8.1 Recommendations for the Future 3D Set-Up

In the autumn 2013, Nuclear Safety Research Unit will have three high speed digital cameras for 3D-imaging. The following suggestions for improvement of the set-up arose:

- Uneven lighting is a problem even with two cameras. If there is only one light source, inevitably at least one side of the bubble will be overexposed and other underexposed, and part of the information will be lost. Different light sources could be tried out. One option could be LED lights immersed into the pool. With suitable fitting, the LED lights might give lighting smooth enough without disturbing the pattern recognition process. Suitable LED lights would probably bear the difficult pressure and temperature circumstances. A light source could be tried to be placed to the ceiling of the wet well pool, so that it is not placed under water. In the easiest situation, if there is enough space, two different light sources in the opposite parts of the pool might help already a lot. Optical fibers could also be tried to get a better lighting.
- Reflections from the steel structures caused errors to the pattern recognition. If the steel structures could be painted matt black, the reflections would decrease and there would still be enough light scattered from the bubbles. The circumstances inside the pool might however be such that

most of the paint could crack and peel off.

- Enclosures of the instrumentation could be made more unnoticeable.
- With three different cameras, one would shoot under the pool and the other two from the sides of the pool in such a way that they are perpendicular to each other. The perpendicularity should be made quite precise, as then there would not be overlapping information, or on the other hand, no important information would be lost.
- The blowdown pipe's outlet should be at the same level as the side cameras.
- Even if the side cameras would be at the same level as the blowdown pipe's outlet, the refractive index of water will cause different magnification of the images if the layer of water is larger in the other direction. If it will be impossible to put the cameras at the same distance from the pipe, some reference object might be used with and without water, so the real magnification will be estimated.
- Tilting the camera will cause aberrations whose evaluation will be hard. If the situation will exist, a similar reference object might be used.
- Different shooting modes and shutter speeds could be tried with and without water.
- When the optimal settings have been found, it would be better to stay with those.
- The cameras should be mounted in such a way that even if they are removed, it is possible to put them back to the same places.
- One or two different settings might be chosen. This may require some hours of testing, but will speed up the experiments in the future.
- There is no use to design a new pattern recognition algorithm before the right settings and the final positions of the cameras have been found.
- With the complex facility, sometimes it is good to realize that a perfect pattern recognition algorithm, which would work in all occasions will be unfeasible and some approximations have to be done.

Bibliography

- [1] Bangash M.Y.H. (editor), 2011. *Structures for Nuclear Facilities - Analysis, Design, and Construction*. New York: Springer.
- [2] Puustinen M., Partanen H., Räsänen A. & Purhonen H., 2007. PPOOLEX Facility Description.
- [3] Räsänen A. & Puustinen M., 2003. POOLEX-esikokeissa käytettävissä olevat mittaukset. In Finnish.
- [4] Laine J. & Puustinen M., 2003. Preliminary Condensation Pool Experiments with Steam Using DN80 and DN100 Blowdown Pipes.
- [5] Laine J. & Puustinen M., 2004. Preliminary Condensation Pool Experiments with Steam Using DN200 Blowdown Pipe.
- [6] Tanskanen V., Puustinen M. & Laine J., 2005–2008. Deliverable D2.1.15.2a: Validation of NURESIM-CFD Against POOLEX Condensation Pool Experiments: Progress report. European Commision, 6th Euratom Framework Programme, Integrated Project: NURESIM Nuclear Reactor Simulations Sub-Project 2: Thermal Hydraulics.
- [7] Puustinen M., Partanen H., Laine J., Räsänen A. & Purhonen H., 2006. Preliminary Plan for a Condensation Pool Test Rig Including a Drywell.
- [8] Puustinen M. & Laine J., 2008. Characterizing Experiments of the PPOOLEX Test Facility.
- [9] Puustinen M., Laine J. & Räsänen A., 2009. PPOOLEX Experiments on Thermal Stratification and Mixing.
- [10] Laine J., Puustinen M., Räsänen A. & Tanskanen V., 2011. PPOOLEX Experiments on Stratification and Mixing in the Wet Well Pool.

-
- [11] Puustinen M., Laine J. & Räsänen A., 2012. PPOOLEX Experiments with a Blowdown Pipe Collar.
 - [12] Tanskanen V., 2012. *CFD Modelling of Direct Contact Condensation in Suppression Pools by Applying Condensation Models of Separated Flow*. Acta Universitatis Lappeenrantaensis 472, Lappeenranta University of Technology.
 - [13] Bordel S., Mato R. & Villaverde S., 2006. Modeling of the evolution with length of bubble size distributions in bubble columns. *Chemical Engineering Science*, **61**, pp. 3663–3673.
 - [14] Laakkonen M., Moilanen P., Alopaeus V. & Aittamaa J., 2007. Modelling local bubble size distributions in agitated vessels. *Chemical Engineering Science*, **62**, pp. 721–740.
 - [15] Jo D. & Revankar S.T., 2011. Investigation of bubble breakup and coalescence in a packed-bed reactor – part 1: A comparative study of bubble breakup and coalescence models. *International Journal of Multiphase Flow*, **37**, pp. 995–1002.
 - [16] Levy E., Wagh M., Sethu H. & Pinarbasi A., 1992. Pattern-Recognition Analysis of Bubbles Impacting on Tubes. *Powder Technology*, **70**, pp. 175–181.
 - [17] Liebenberg L., Thome J.R. & Meyer J.P., 2005. From Visualization and Flow Pattern Identification With Power Spectral Density Distributions of Pressure Traces During Refrigerant Condensation in Smooth and Microfin Tubes. *Journal of Heat Transfer*, **127**, pp. 209–220.
 - [18] Laine J., Puustinen M. & Räsänen A., 2013. PPOOLEX Experiments of the Dynamics of Free Water Surface in the Blowdown Pipe.
 - [19] Räsänen A., 2004. *Mittausjärjestelmä lauhtumisilmiöiden tutkimukseen*. Diplomityö, Lappeenrannan teknillinen yliopisto. In Finnish.
 - [20] Li H. & Kudinov P., 2009. GOTHIC code simulation of thermal stratification in POOLEX facility. QC 20120207.
 - [21] Lahey R. & Moody F., 1993. *The Thermal-Hydraulics of a Boiling Water Reactor*. 2nd edition edition. American Nuclear Society.
 - [22] MATLAB R2011b. Version 7.13.0.564.

- [23] Theodoridis S., Pikrakis A., Koutroumbas K. & Cavouras D., 2010. *Introduction to Pattern Recognition: A MATLAB Approach*. 1st edition edition. Elsevier Inc.
- [24] ImageJ, Image Processing and Analysis in Java. URL <http://rsbweb.nih.gov>. Version 1.46.
- [25] Audio Video to Picture Converter. URL www.aoaophoto.com. Version 2.9.
- [26] Otsu N., 1979. A Threshold Selection Method from Gray-level Histograms. *IEEE Transactions on Systems, Man, and Cybernetics*, **9**(1), pp. 62–66.
- [27] Hecht E., 2002. *Optics*. 4th edition edition. Addison-Wesley.
- [28] Young H.D., Freedman R.A. & Ford L., 2007. *University Physics*. 12th edition edition. Addison-Wesley.
- [29] Ross H.E., Franklin S.S., Weltman G. & Lennie P., 1970. Adaptation of Divers to Size Distortion Under Water. *Br. J. Psychol.*, **61**(3), pp. 365–373.
- [30] Dhawan A.P., 2011. *Medical Image Analysis*. New Jersey: Wiley-IEEE Press.
- [31] Harrison L., 2011. *Clinical Applicability of MRI Texture Analysis*. Acta Universitatis Tamperensis 1640, University of Tampere.

Appendix I Test Vessel Measurements

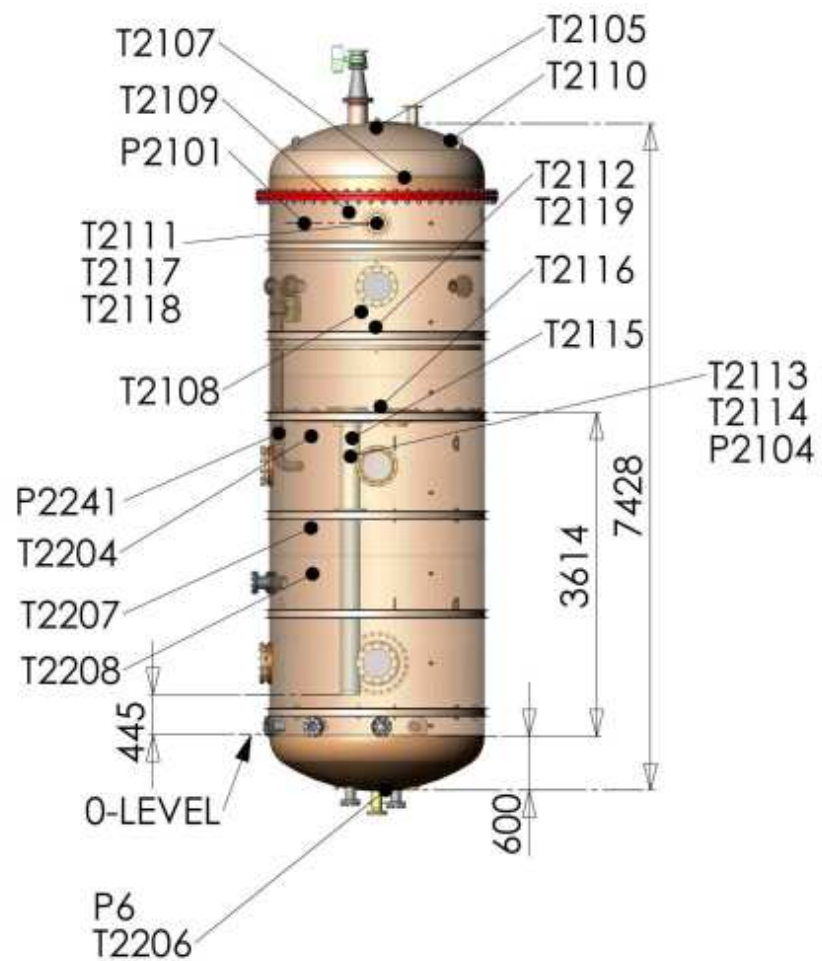


Figure I.1. Test vessel measurements.

Appendix II Temperature Measurements

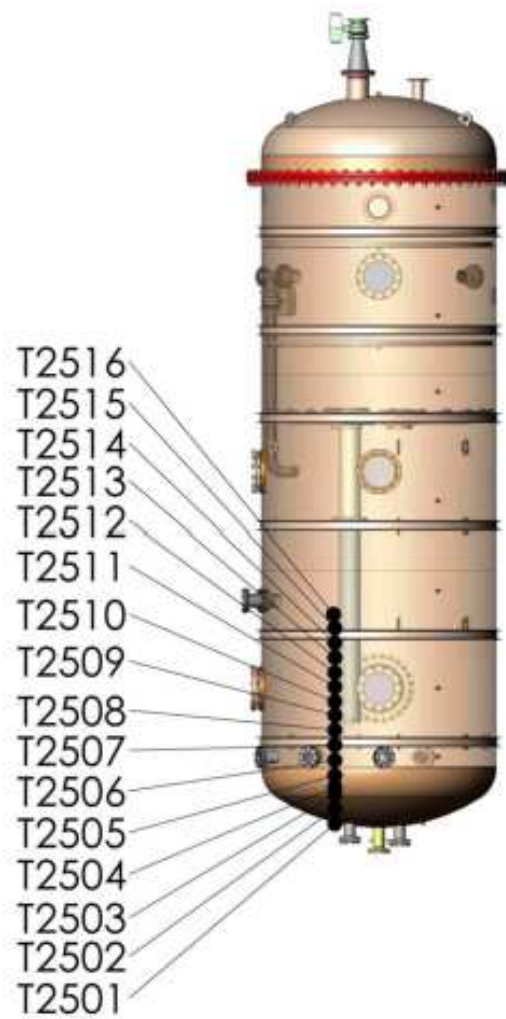


Figure II.1. Temperature measurements in the wet well pool for the detection of thermal stratification.

Appendix III Flow Diagram

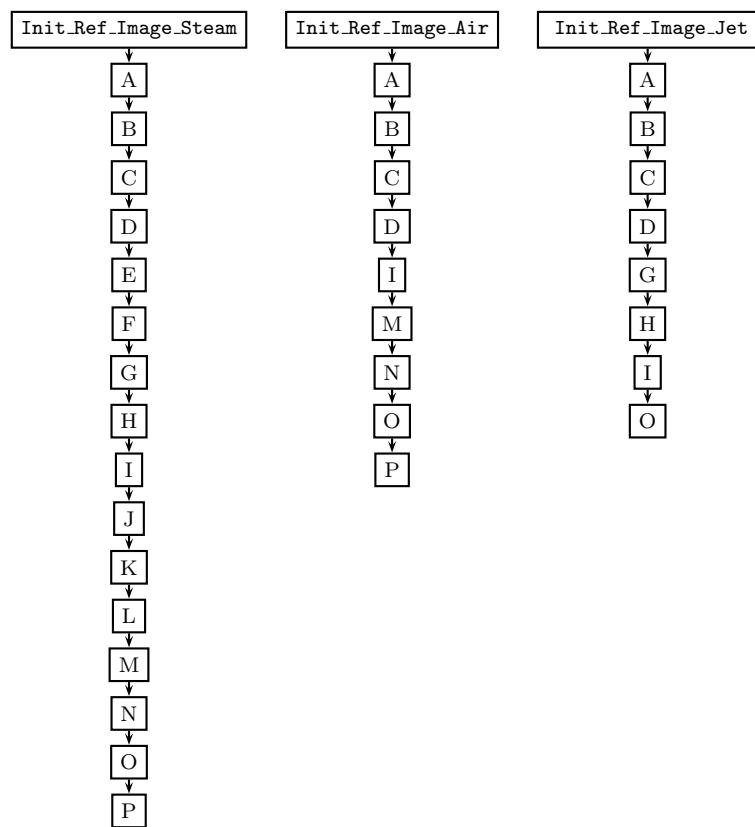


Figure III.1. Flow diagram of `Init_Ref_Image_(Steam/Air/Jet)` functions

Appendix IV 1 second of Air Bubbles

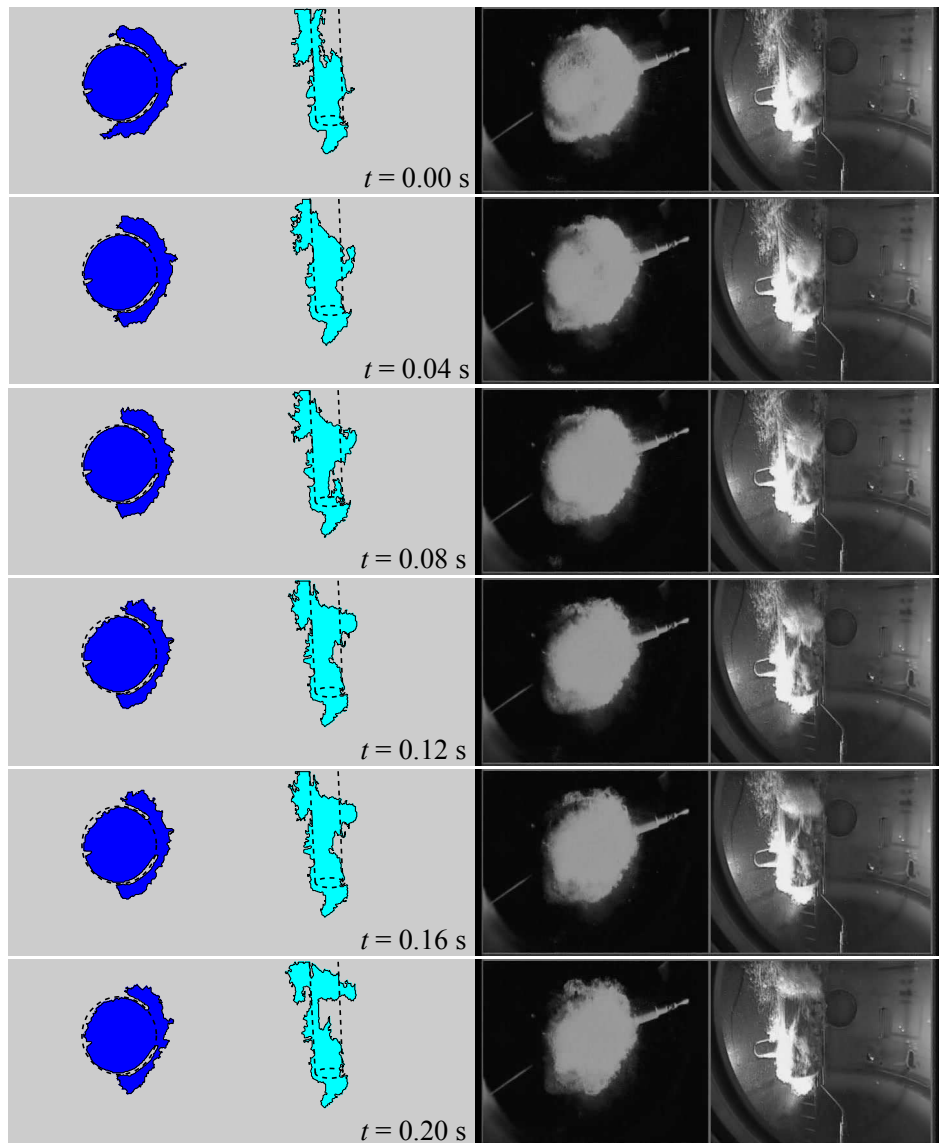


Figure IV.1. Air bubbles during the time 0.00–0.20 s.

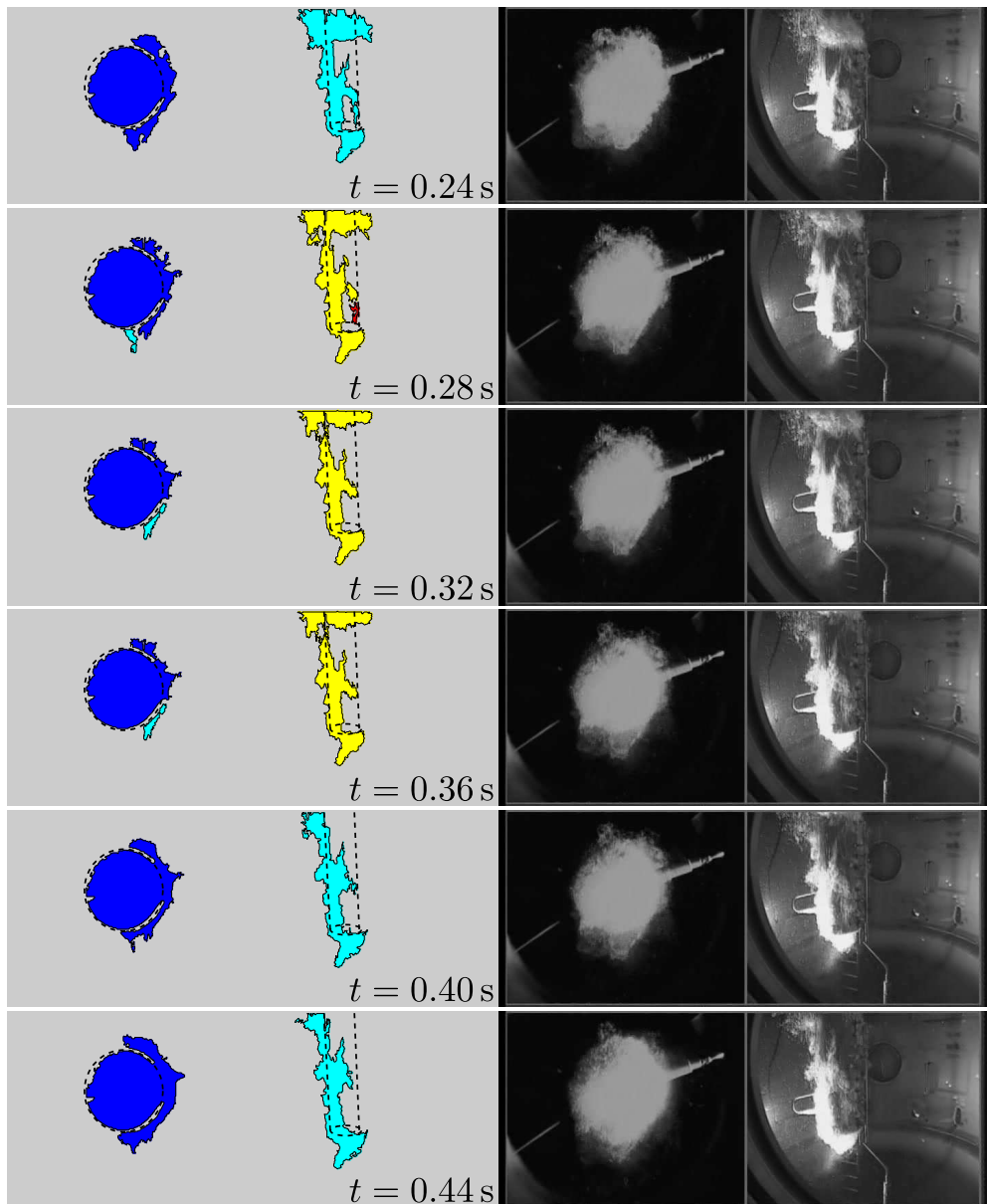


Figure IV.2. Air bubbles during the time 0.24–0.44 s.

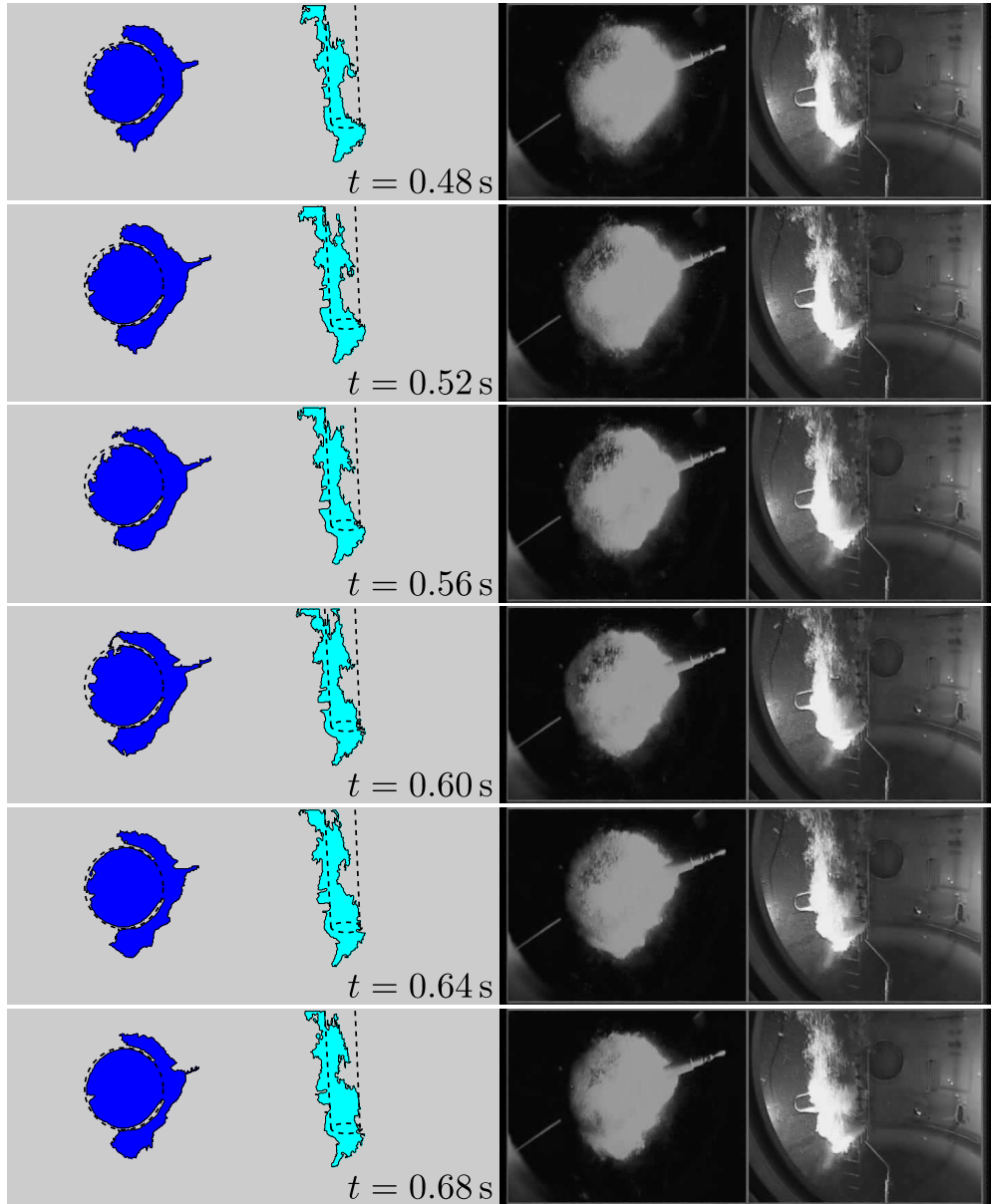


Figure IV.3. Air bubbles during the time 0.48–0.68 s.

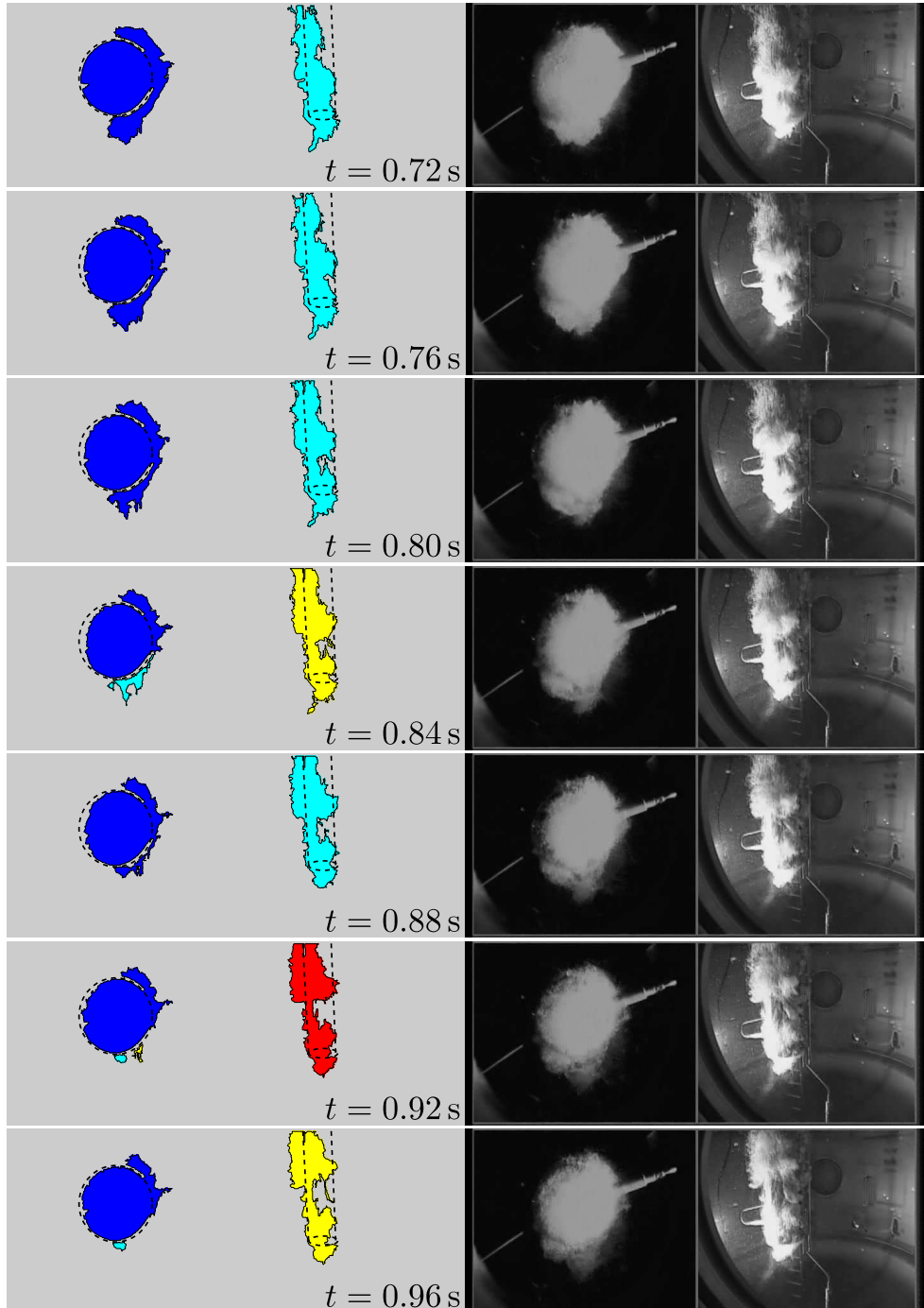


Figure IV.4. Air bubbles during the time 0.72–0.96 s.

Appendix V 1 second of Steam Bubbles

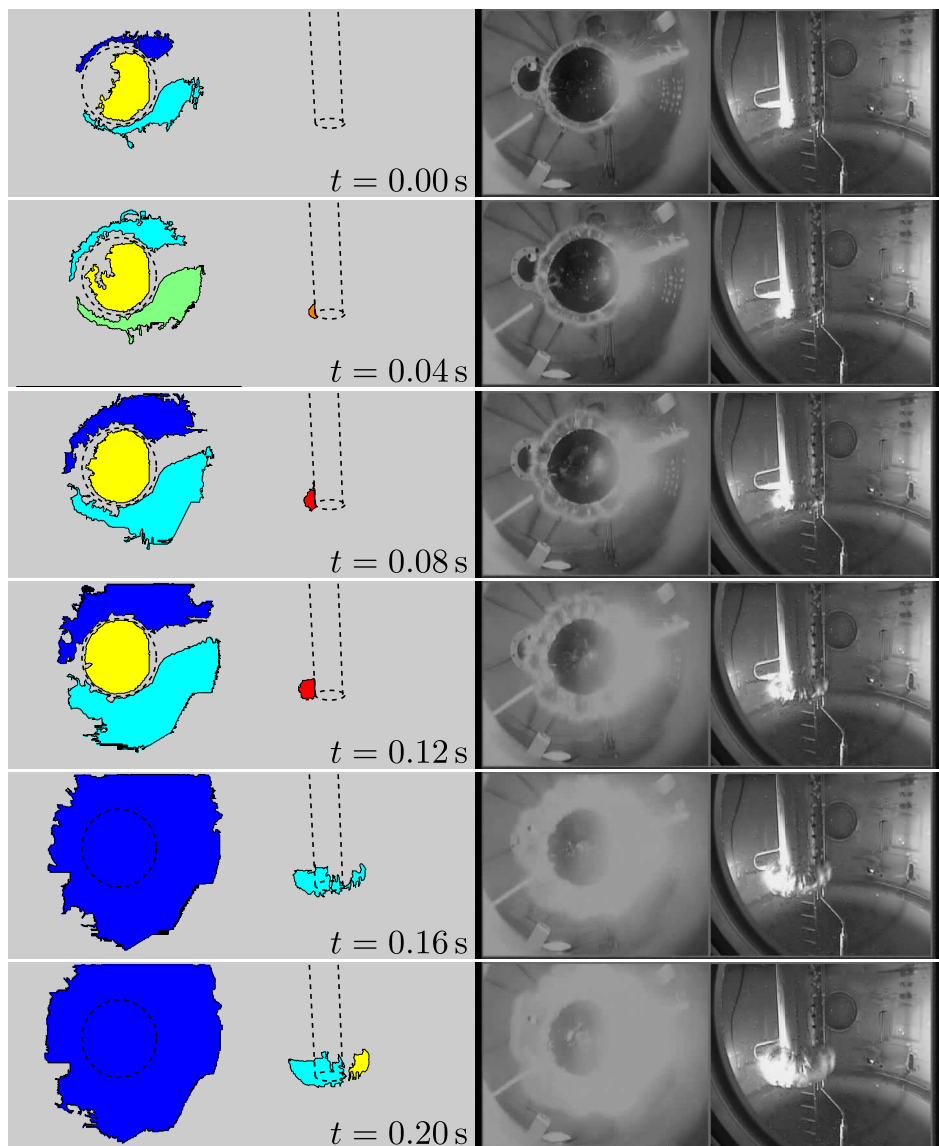


Figure V.1. Steam bubbles during the time 0.00–0.20 s.

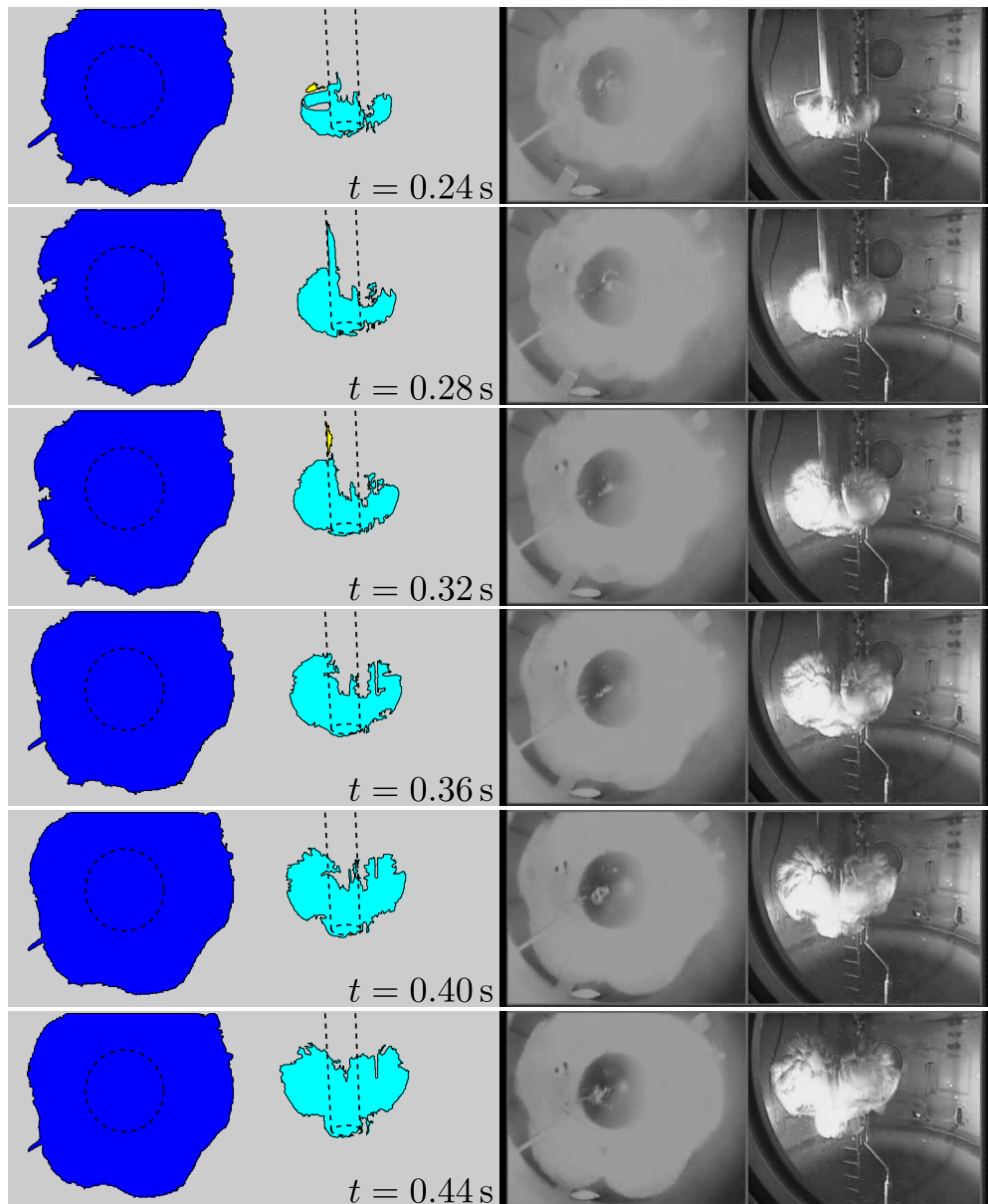


Figure V.2. Steam bubbles during the time 0.24–0.44 s.

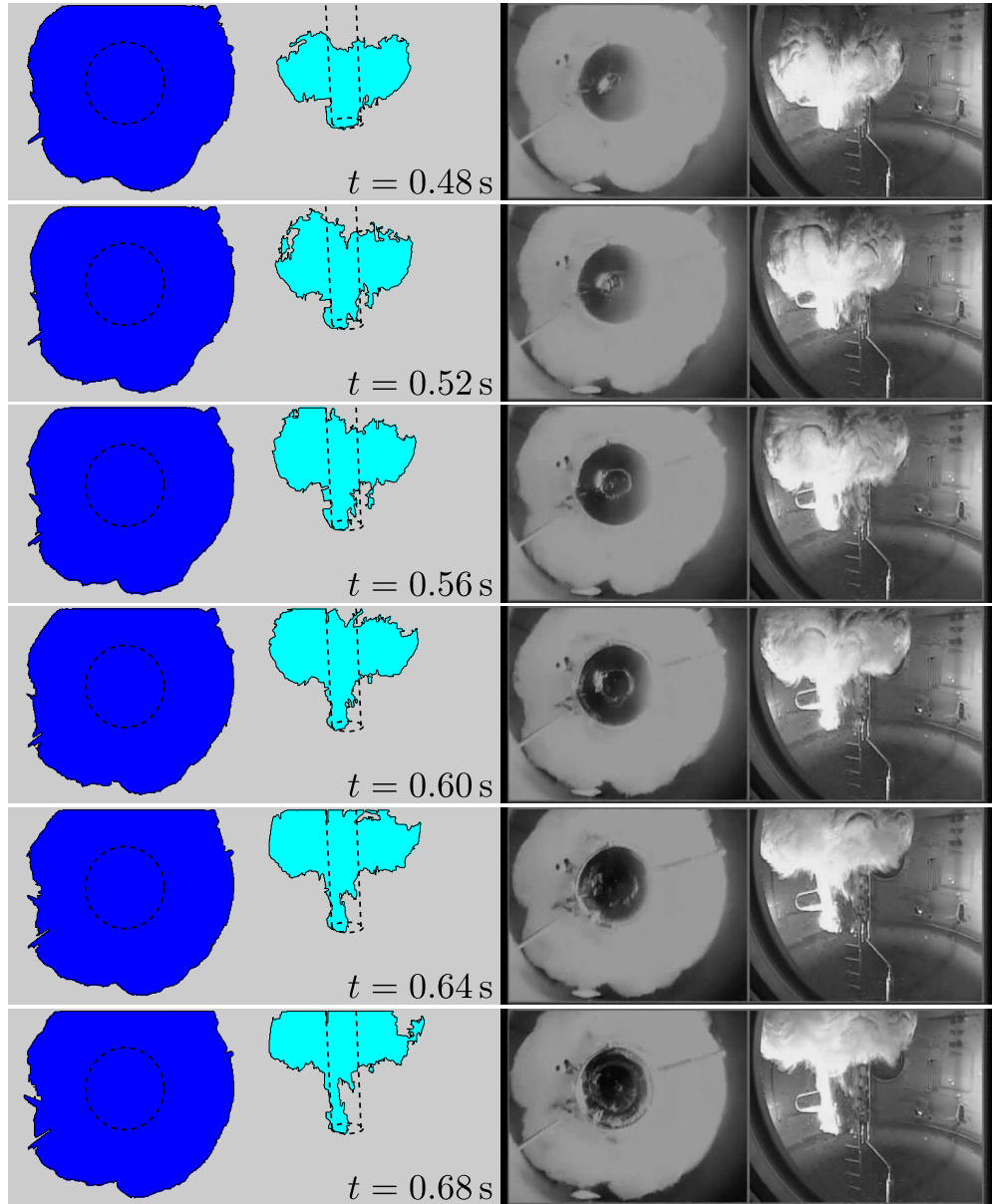


Figure V.3. Steam bubbles during the time 0.48–0.68 s.

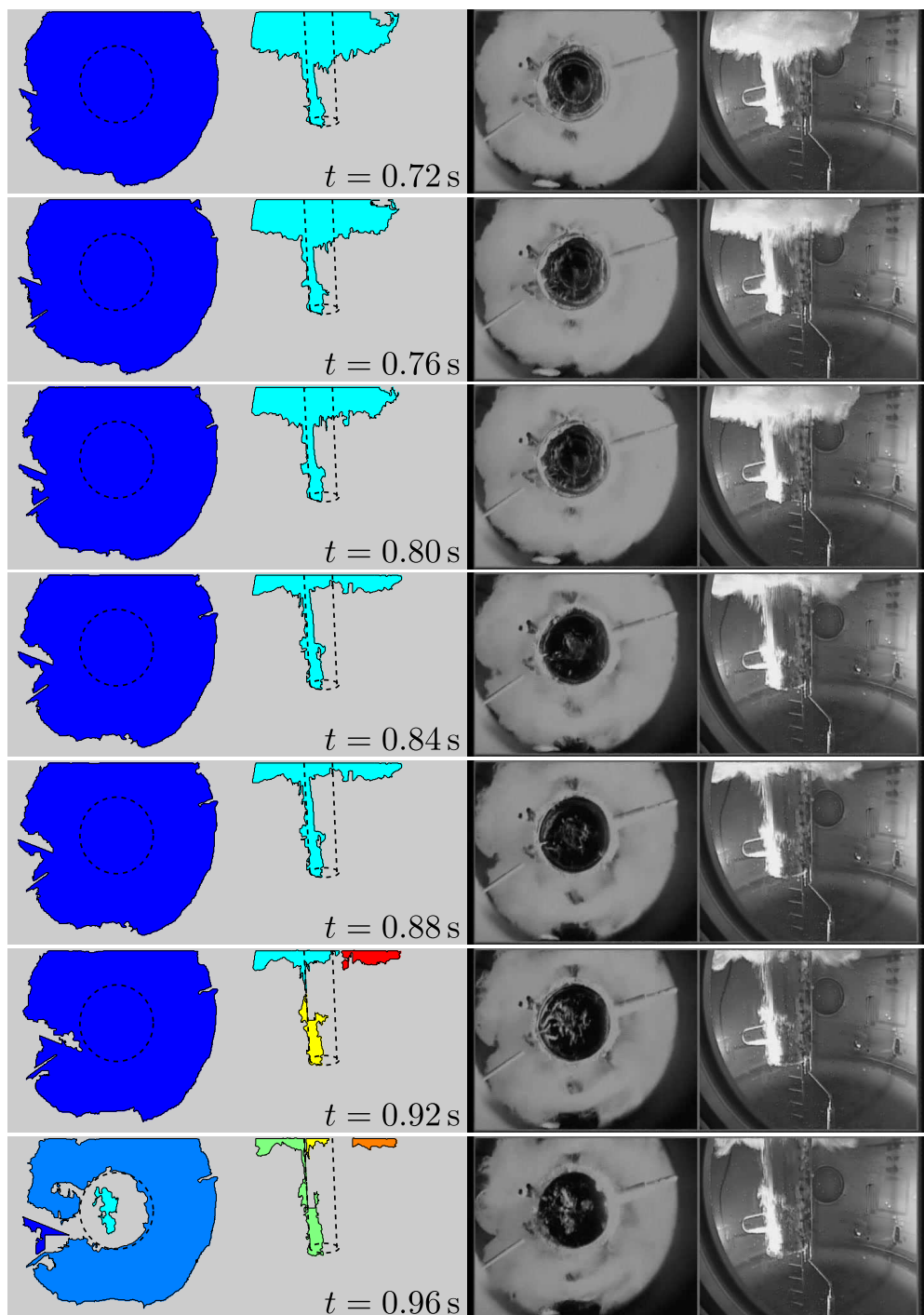


Figure V.4. Steam bubbles during the time 0.72–0.96 s.

Appendix VI 1 second of Jets

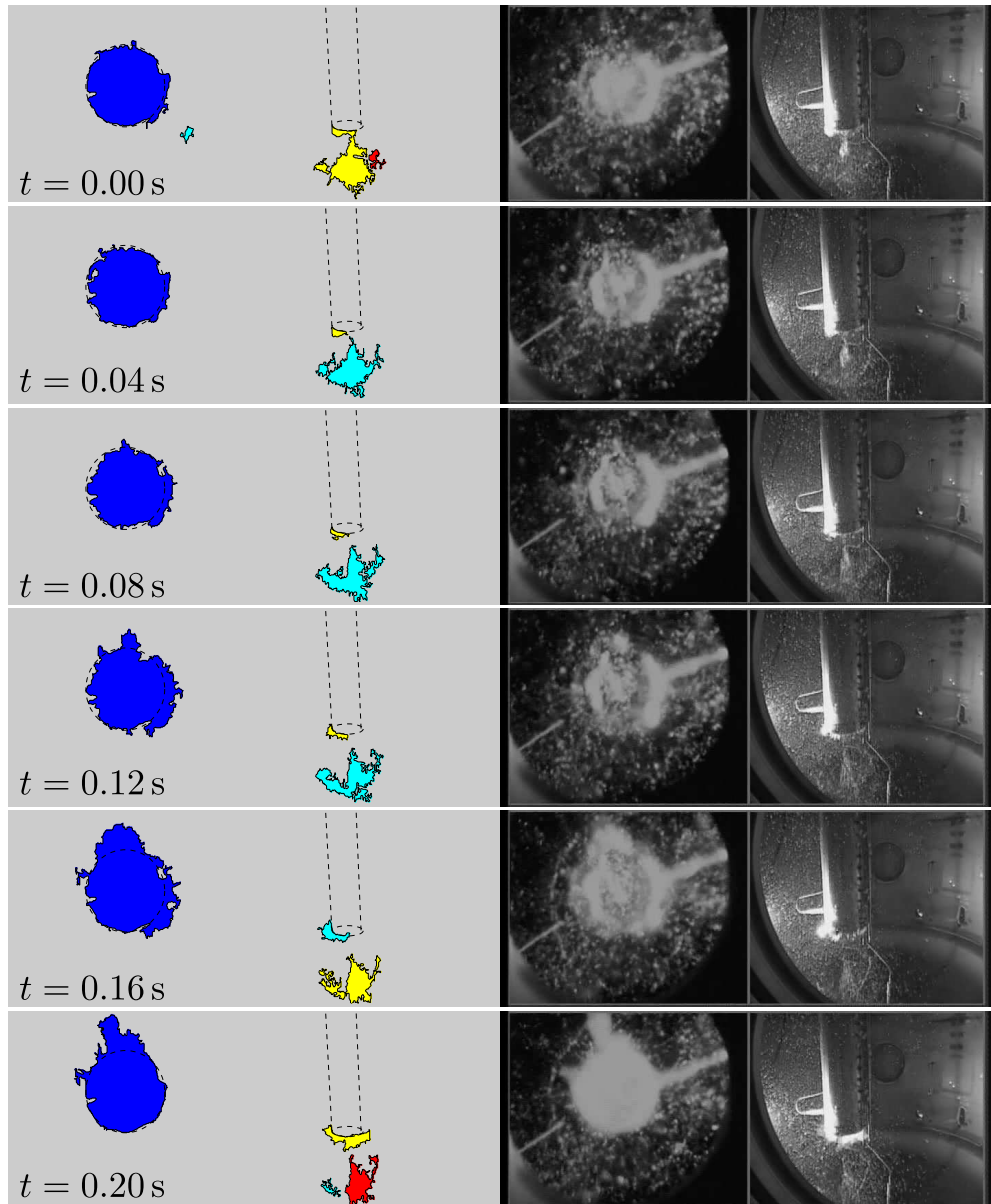


Figure VI.1. Jets during the time 0.00–0.20 s.

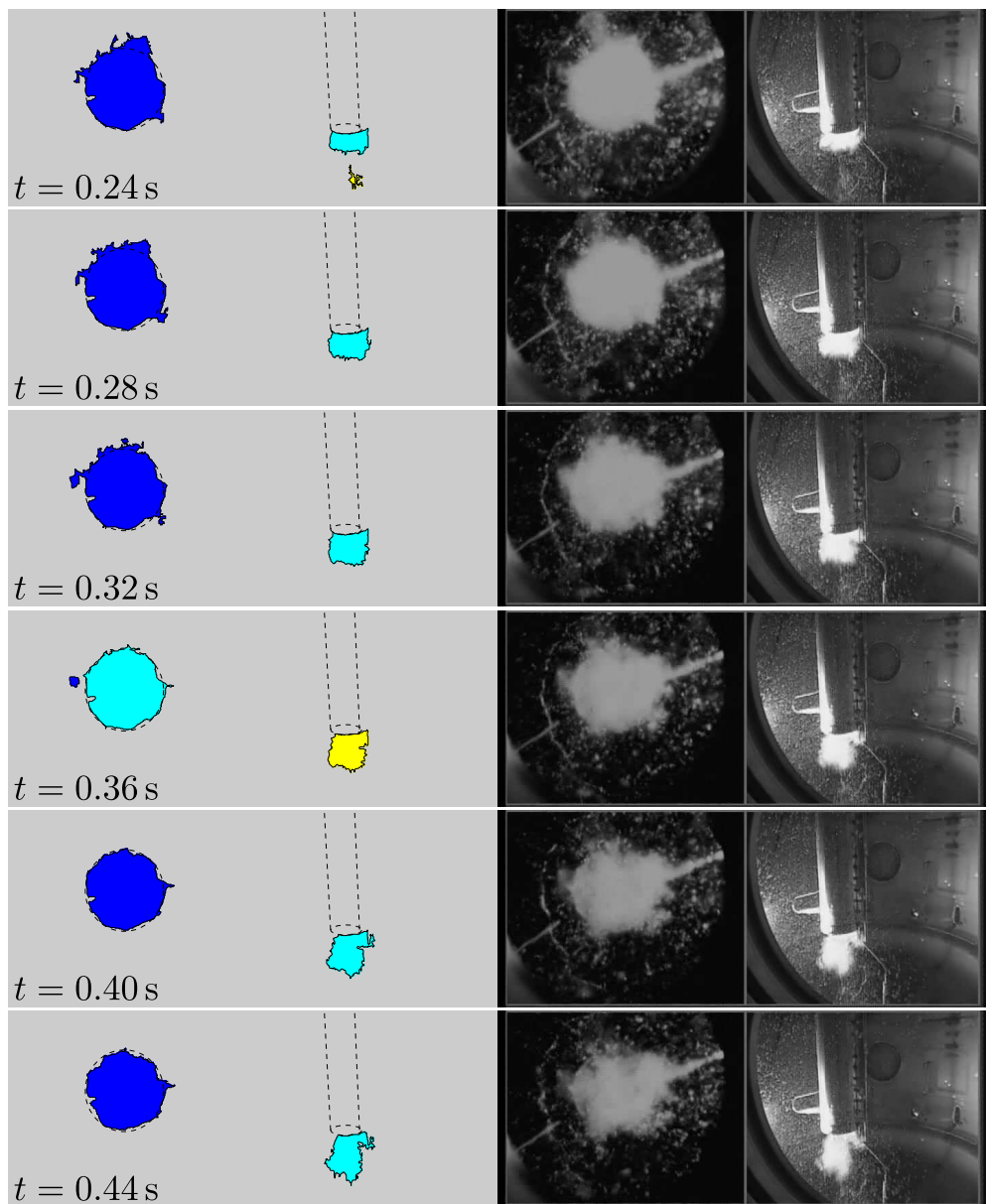


Figure VI.2. Jets during the time 0.24–0.44 s.

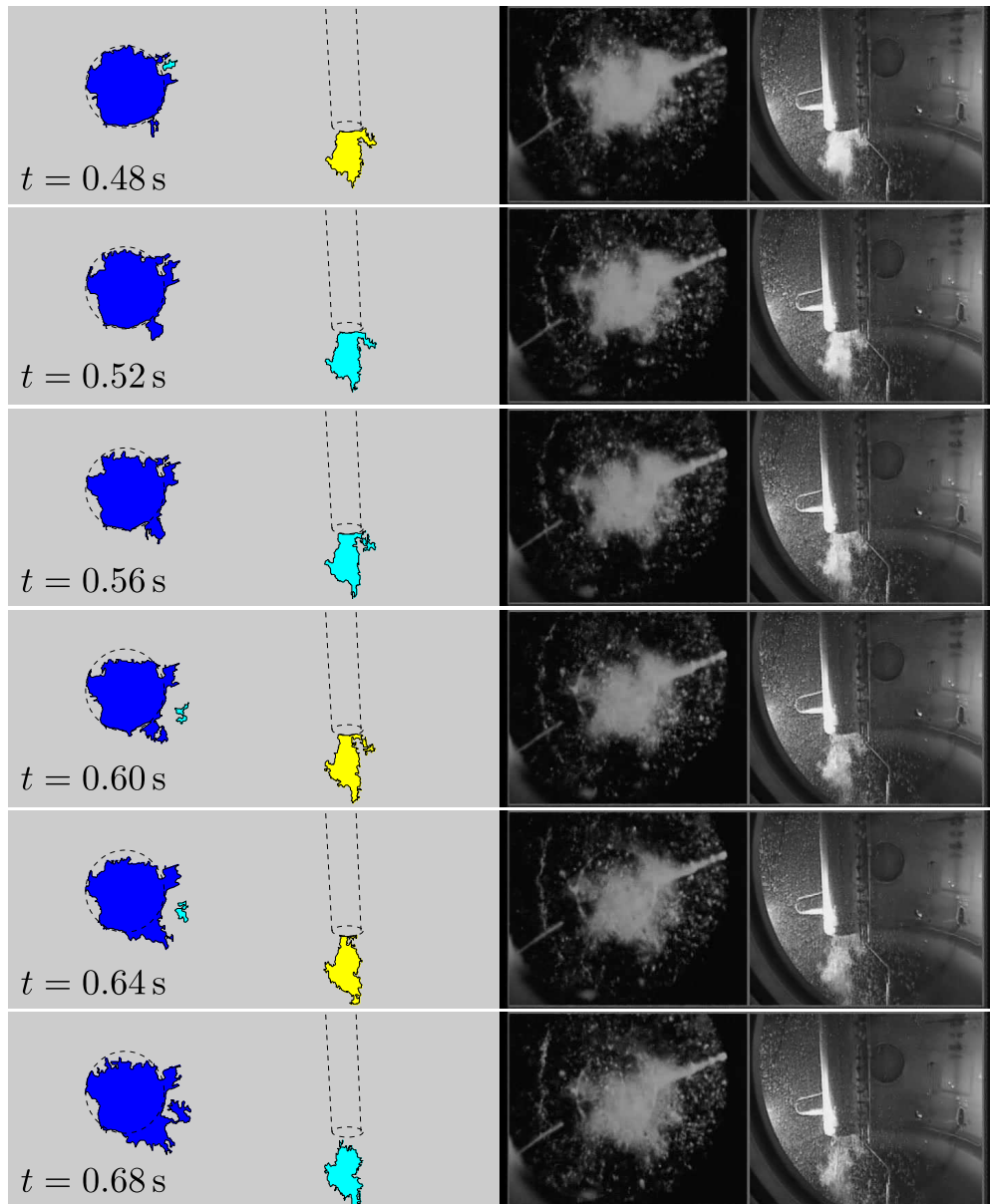


Figure VI.3. Jets during the time 0.48–0.68 s.

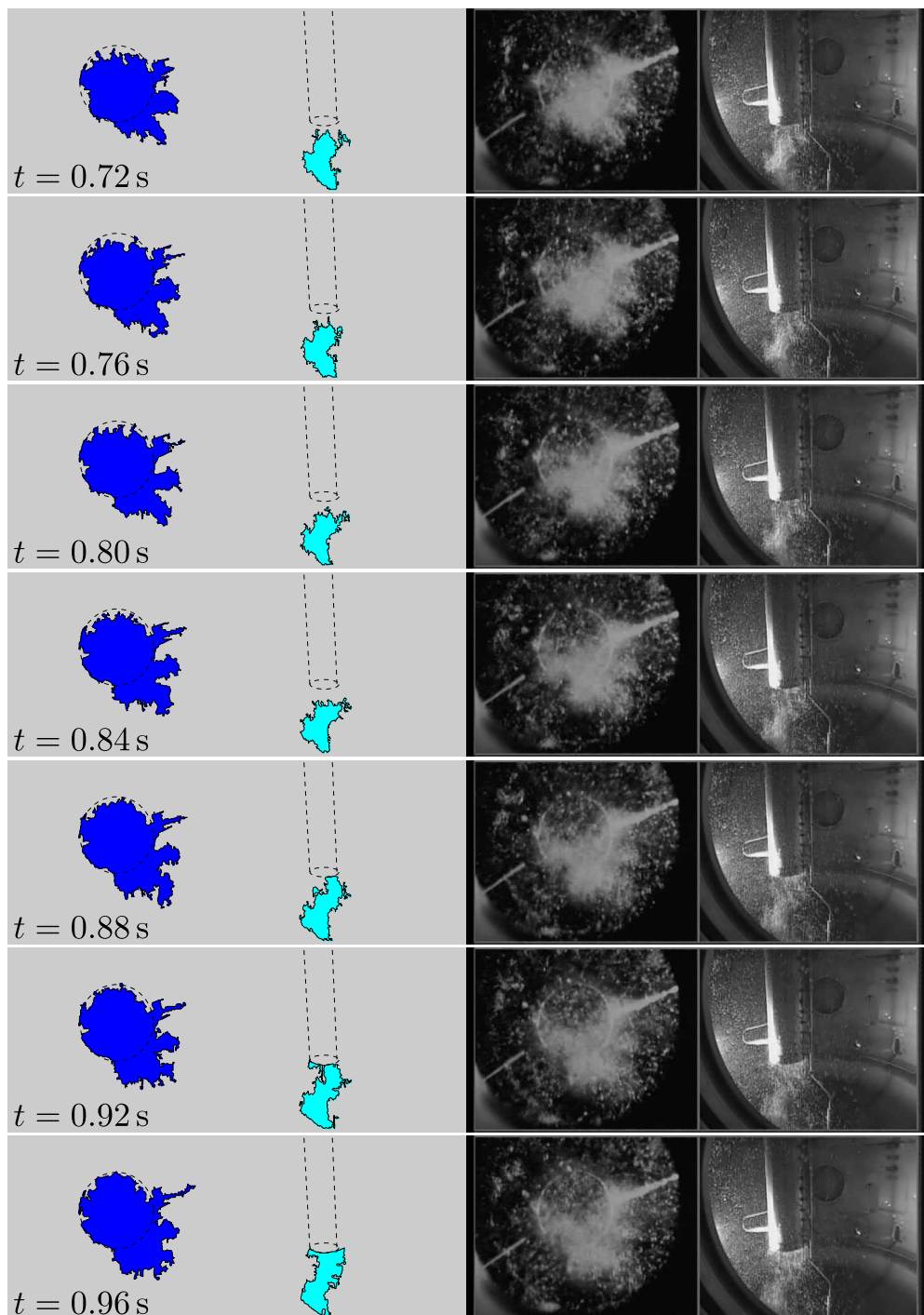


Figure VI.4. Jets during the time 0.72–0.96 s.